



Abstract

18 The relative importance of changes in radiative forcing (downwelling longwave radiation) and
19 mechanical mixing (20 m wind speed) in controlling boundary layer stability annually and seasonally at
20 five study sites across the Antarctica continent is presented. From near-neutral to extremely strong near-
21 surface stability, radiative forcing decreases with increasing stability, as expected, and is shown to be a
22 major driving force behind variations in near-surface stability at all five sites. Mechanical mixing usually
23 decreases with increasing near-surface stability for regimes with weak to extremely strong stability. For
24 the cases where near-neutral, very shallow mixed, and weak stability occur, the wind speed in the very
25 shallow mixed case is usually weaker compared to the near-neutral and weak stability cases while
26 radiative forcing is largest for the near-neutral cases. This finding is an important distinguishing factor for
27 the unique case where a very shallow mixed layer is present, indicating that weaker mechanical mixing in
28 this case is likely responsible for the shallower boundary layer that defines the very shallow mixed
29 stability regime. For cases with enhanced stability above a layer of weaker near-surface stability, lower
30 downwelling longwave radiation promotes the persistence of the stronger stability aloft, while stronger
31 near-surface winds act to maintain weaker stability immediately near the surface, resulting in this two-
32 layer boundary layer stability regime.



33 1 Introduction

34 The atmospheric boundary layer is the lowest part of the atmosphere where the surface of the
35 earth and overlying atmosphere interact, for example, exchanging heat and moisture. Boundary layer
36 stability varies based largely on the surface energy budget and mechanical mixing driven by wind shear.
37 Increased downwelling longwave radiation, in the presence of cloud cover, or solar radiation reduces
38 boundary layer stability, while clear skies, with less downwelling longwave radiation, and long periods of
39 darkness, especially in the polar regions, allows for the formation of strong near-surface temperature
40 inversions (King and Turner 1997; Cassano et al., 2016). Increased near surface wind speed, and thus
41 wind shear, can also reduce stability by generating turbulence and mixing down warmer air from aloft. In
42 contrast, weak winds and reduced wind shear and mixing allow for stronger near-surface stability
43 (Hudson and Brandt, 2005; Dice and Cassano, 2022). Here, we will use the findings from Dice et al.
44 (2023), which described the range of boundary layer stability present at two continental interior and three
45 coastal sites in Antarctica (Figure 1), to determine how radiative forcing and mechanical mixing vary
46 across this range of boundary layer stability regimes, and how these mechanisms vary seasonally and
47 across the continent.

48 Previous boundary layer studies have widely documented radiative forcing and wind shear to be
49 two main drivers of variations in static stability in the boundary layer (Hudson and Brandt, 2005; Stone
50 and Kahl, 1991; King and Turner, 1997; etc.). In terms of radiative forcing, Cassano et al. (2016) found a
51 strong seasonal cycle of inversion strength over the Ross Ice Shelf, approximately 100 km from
52 McMurdo, with stronger inversion strength in the austral winter during polar night while solar radiation is
53 zero, and weaker inversion strength in the austral summer during polar day when the sun is always above
54 the horizon and solar heating is strongest. Dice and Cassano (2022) also found decreasing radiative flux
55 with increasing stability at McMurdo. At Neumayer, Silva et al. (2022) noted strong temperature
56 inversions, especially during the winter when solar radiation is low or zero during polar night. Hudson
57 and Brandt (2005) found that inversion strength decreases with increasing radiative flux in the winter at
58 South Pole and Dome Concordia (“Dome C”). This was also observed by Pietroni et al. (2013), who
59 found the strongest surface-based temperature inversions at Dome C to occur with strong radiative
60 cooling, which is at its maximum in the austral winter. Further, increased downwelling longwave
61 radiation is usually associated with reduced near-surface stability in the Arctic (Solomon et al., 2023) and
62 Antarctic (Stone and Kahl, 1991; Dice and Cassano, 2022).

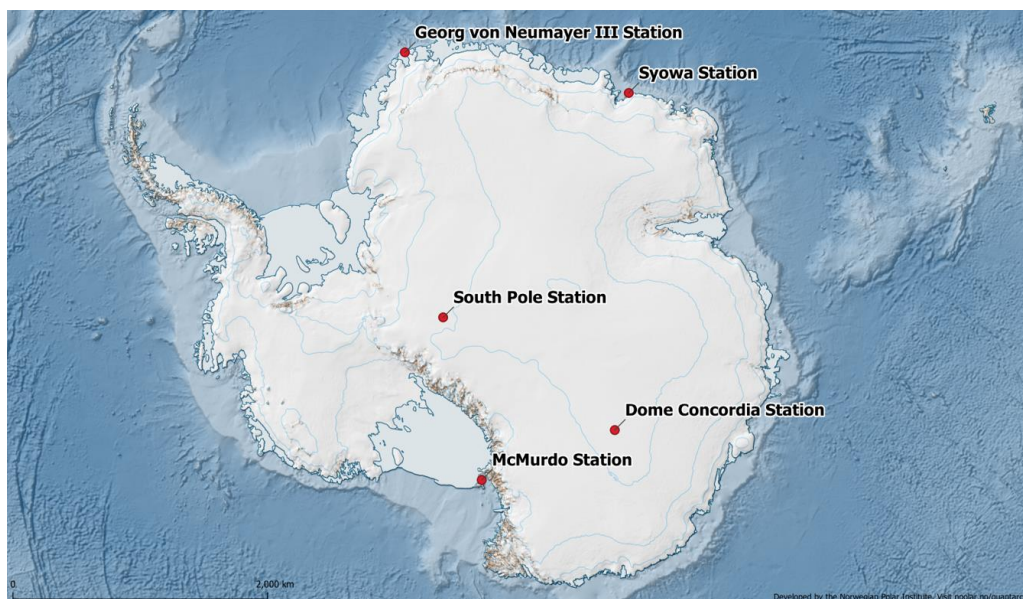
63 When analyzing boundary layer stability in terms of variations in near-surface wind speed,
64 Cassano et al. (2016) found that over the Ross Ice Shelf, the strength of inversions is related to the
65 strength of the wind speed, with the strongest inversions occurring when the wind speed is less than 4 m s^{-1}
66 $^{-1}$, and the strength of the inversion rapidly decreases with increasing winds above 4 m s^{-1} . Dice and
67 Cassano (2022) found the strongest inversions occurring with wind speeds less than 4.3 m s^{-1} at
68 McMurdo. Silva et al. (2022) investigated boundary layer stability at Neumayer, and found strong
69 inversions were associated with low wind speeds. Hudson and Brandt (2005) found that, while it is
70 generally expected that increasing wind speeds will reduce near-surface stability by mixing warmer air
71 from aloft to the surface, the strongest stability conditions occur when wind speeds are 3 m s^{-1} to 5 m s^{-1}
72 rather than calm at South Pole and Dome C, which was also noted by other studies in the coastal regions
73 of Antarctica (Cassano et al., 2016). Results from Argentini et al. (2005) show that a wind speed of 4.5 m s^{-1}
74 $^{-1}$ is required to reduce stable conditions to well mixed conditions at Dome C and Pietroni et al. (2013)
75 found the strongest surface-based temperature inversions at Dome C occur with weak winds.

76 In addition to radiative forcing and mechanical mixing, several other phenomena can alter the
77 static stability in the boundary layer. For example, temperature advection or warm air from over open



78 water or cold air from over ice sheets or sea ice can quickly change near-surface stability conditions
79 especially at coastal locations such as McMurdo, Neumayer, and Syowa. Warm air advection over a cold
80 surface would result in increased near-surface stability (Stone and Kahl, 1991; Vignon et al., 2017;
81 Pietroni et al., 2013). It is also possible that cyclonic activity can alter near-surface boundary layer
82 stability, through changes in wind speed and cloud cover associated with the cyclone. At Neumayer,
83 cyclonic activity reaches a maximum in the fall and spring, during which temperature inversions are
84 rarely observed, whereas during non-cyclonic periods, temperature inversions are observed three times as
85 often compared to during the cyclonic periods (Silva et al., 2022). Additionally, katabatic flow from the
86 continental interior has been observed to impact conditions at Syowa and can flow from the plateau
87 located just above the South Pole as well. At Syowa, there is a high frequency of strong wind events
88 associated with katabatic activity in the fall and winter (Yamada and Hirasawa, 2018). The effects of
89 katabatic flow on boundary layer stability at Syowa is not well documented, but katabatic flow can either
90 result in the influx of cold air near the surface, resulting in strong temperature inversions, or increased
91 mechanical mixing can reduce near-surface stability (Vihma et al., 2011). At South Pole, clear-sky
92 conditions are associated with weak katabatic flow from the plateau, resulting in a persistent and strong
93 surface-based temperature inversion (Stone and Kahl, 1991).

94 The results presented below will assess differences in radiative forcing, as shown by downwelling
95 longwave radiation, and mechanical generation of turbulence, as shown by near-surface wind speed,
96 associated with varying boundary layer stability across the Antarctic continent (Section 3). The relative
97 importance of forcing mechanisms for the various regimes annually and seasonally and across the
98 continent will be explored in Section 4.



99 *Figure 1: As seen in Dice et al. (2023): Map locations of all study sites (red dots with station names)*
100 *across the continent. Map courtesy of Quantarctica (Matsuoka et al., 2018).*



101 2 Data and Methods

102 2.1 Data

103 Radiosonde data from two continental interior sites (South Pole and Dome C) and three coastal
104 sites (McMurdo, Neumayer, and Syowa) (Figure 1, Table 1) as well as corresponding downwelling
105 longwave radiation data at the time the radiosonde launches occurred are included in this analysis. As
106 described by Dice et al. (2023), the lengths of data sets (13 months at McMurdo to 19 years at Syowa) are
107 used for the data presented here, reflecting the longest term, continuous, and easily accessible data set
108 from each of the five sites listed above. The shorter period of data from McMurdo is used to coincide with
109 availability of radiosonde and radiation data from the year-long Department of Energy Atmospheric
110 Radiation Measurement (ARM) West Antarctic Radiation Experiment (AWARE) (Lubin et al., 2017,
111 2020; Silber et al., 2018) campaign, which was also previously analyzed by Dice and Cassano (2022) and
112 Dice et al. (2023). The data from Neumayer station is also a relatively shorter data set, as data with high
113 enough resolution was not available until 2018 (Dice et al., 2023). The data sets at South Pole, Dome C,
114 and Syowa have data available spanning more than at least 15 years.

115 Located 2835 m above sea level, South Pole is a high elevation continental interior site known for
116 its persistent cold conditions and temperature inversions (Zhang et al., 2011; Hudson and Brandt, 2005;
117 etc.). Radiosonde data from 1 January 2005 through 29 September 2021 have been retrieved from the
118 Antarctic Meteorological Research and Data Center (AMRDC). The radiosondes at South Pole are
119 launched once per day at 2100 UTC, and twice per day during the austral summer when conditions allow.
120 The radiative flux data from South Pole are from the Baseline Surface Radiation network (BSRN), and
121 the instrumentation for this data is located 0.8 km away from the radiosonde launch site (Table 1).

122 Also located at high elevation, at 3233 m above sea level, Dome C is located on a plateau with a
123 nearly flat surface around it, characterized by almost constant near-surface temperature inversions and
124 strong stability (Genthon et al., 2013; Pietroni et al., 2013). Radiosonde data from Dome C between 21
125 January 2006 and 14 October 2021 are from the Antarctic Meteo-Climatological Observatory, and
126 radiosonde launches are performed once per day throughout the year at 1200 UTC. Radiation data from
127 Dome C was obtained from BSRN, and the site of the radiation instrumentation is located 0.6 km away
128 from the radiosonde launch site (Table 1).

129
130 Located on Hut Point Peninsula of Ross Island, McMurdo is a coastal site surrounded by complex
131 topography, where Mt. Erebus rises to 3,794 m. McMurdo is located between McMurdo Sound to the
132 west and north and the Ross Ice Shelf to the south and east. The data used in this study from McMurdo
133 are from the AWARE campaign (Lubin et al., 2017, 2020; Silber et al., 2018), which occurred at
134 McMurdo from 20 November 2015 to 3 January 2017. During AWARE, radiosonde launches occurred
135 twice daily at 1000 UTC and 2200 UTC. The surface radiative flux data from AWARE were recorded
136 approximately 2 km away from the radiosonde launch site (Table 1). The radiosonde site is characterized
137 by coastal influences from McMurdo Sound, with slower wind speeds and warmer temperatures, whereas
138 higher wind speeds and colder temperatures are characteristic of the higher elevation observation site on
139 the Ross Ice Shelf side of the Hut Point peninsula where the surface radiation was measured during
140 AWARE (Dice and Cassano, 2022)

141 Located near sea-level on the Ekström Ice Shelf, Neumayer is characterized by flat and
142 homogeneous terrain. Neumayer is influenced by cyclone activity in the circumpolar trough, which can
143 act to quickly impact boundary layer stability at this site (Silva et al., 2022). Radiosonde and surface
144 radiative flux data from Neumayer Station are from BSRN, recorded from 1 June 2018 to 31 January
145 2021, with radiosonde launches occurring once per day at 1200 UTC, and when conditions are favorable



146 during austral summer, a second launch occurs at 0500 UTC. The site of the instrumentation for the
147 radiative flux data is located 3.1 km away from the radiosonde launch site (Table 1).

148 Syowa station is located near sea level on East Ongul Island in the Lutzow-Holm Bay, where the
149 wind and weather conditions are impacted by cyclone activity and katabatic winds from the continental
150 interior (Murakoshi, 1958; Yamada and Hirasawa, 2018). Radiosonde data from 1 February 2001 through
151 23 January 2020 are from the Office of Antarctic Observation Japan Meteorological Agency (pers. comm.
152 Yutaka Ogawa). The radiosonde launches occur twice pre day at 1130 UTC and 2330 UTC. The surface
153 radiative flux data is from BSRN, and the instrumentation for this data is located 1.1. km away from the
154 radiosonde launch site (Table 1).

155 The radiosonde observations from all five sites will be analyzed from 20 m above ground level
156 (AGL) to 500 m AGL. The height of 20 m was chosen as the lowest height to analyze, as oftentimes,
157 warm biases near the surface in radiosonde data are observed below this height, due to radiosondes being
158 moved from warm buildings to outside without enough time to equilibrate to outside temperatures before
159 launch (Schwartz and Doswell, 1991; Mahesh et al., 1997). The height of 500 m was chosen to be the top
160 of the profiles we will analyze here, as the depth of the boundary layer was below 500 m in most cases
161 (Dice and Cassano, 2022; Dice et al., 2023). The boundary layer stability profiles in this study will be
162 assessed based on the vertical potential temperature gradient from each radiosonde profile.

163 Given the two separate locations of the radiosonde launch sites and the surface observation site, it
164 is important to note that these two locations could have slightly different meteorological conditions. For
165 this reason, and because several of the sites have different heights at which surface wind speed is
166 recorded, the surface wind speeds discussed in this study will be near-surface 20 m wind speeds taken
167 from the radiosonde observations rather than surface wind speeds from the respective surface observation
168 sites.



169 *Table 1: Information for each of the five study sites: South Pole, Dome C, McMurdo, Neumayer, and*
 170 *Syowa. From left to right, the columns indicate: study site, latitude, longitude and elevation above sea*
 171 *level (ASL), site location type, distance between the location of the radiosonde launches and the location*
 172 *of the surface observation instrumentation, the type of radiosonde and accuracy of the temperature and*
 173 *wind measurements, respectively, the radiation instrumentation and accuracy, the time period of the*
 174 *radiosonde and radiation data, and the number of radiosonde launches in the dataset.*

Station	Latitude, Longitude, Elevation	Site Type	Distance between Observations	Radiosonde Type and Accuracy	Radiation Instrument and Accuracy	Time Period of Surface Observations	Number of Profiles
South Pole	-89.98°S, 24.80°W; 2,836 m	Interior plateau	811.8 m	Vaisala RS41-SGP radiosondes; 0.2 K, 0.5 m s ⁻¹	Pyrgeometer, Eppley, PIR; 5 W m ⁻²	01 Jan 2005-29 Sep 2021	8,587
Dome Concordia	-75.10°S, 123.33°E; 3,251 m	Interior plateau	571.8 m	RS-92 radiosondes; 0.2 K, 0.2 m s ⁻¹	Pyrgeometer, Kipp & Zonen, CG4; <7.5 W m ⁻²	21 Jan 2006-14 Oct 2021	5,147
McMurdo	-89.98°S, 24.80°W; 2,836 m	Coastal; Ross Island	1.7 km	RS-92 radiosondes; 0.2 K, 0.2 m s ⁻¹	Pyrgeometer, Eppley, PIR; 5 W m ⁻²	30 Nov 2015-03 Jan 2017	8,587
Georg von Neumayer	-70.65°S, -8.17°W; 38 m	Coastal; Ekström Ice Shelf	3.1 km	Vaisala, RS41-SGP radiosondes; 0.2 K, 0.5 m s ⁻¹	Pyrgeometer, Eppley, PIR; 5 W m ⁻²	01 Jun 2018-31 Jan 2021	1,220
Syowa	-69.00°S, 39.58°W; 18.4 m	Coastal; East Ongul Island	1.1 km	Meisei RS-11G radiosondes; 0.5 K, 2 m s ⁻¹	Pyrgeometer, Kipp & Zonen, CG4; <7.5 W m ⁻²	01 Feb 2007-23 Jan 2020	6,390

175 **2.2 Methods**

176 **2.2.1 Definition Scheme for Boundary Layer Stability Regimes**

177 Boundary layer stability regimes, accounting for both near-surface stability and stability above
 178 the boundary layer, were defined by Dice et al. (2023) (Table 2) and used to classify the stability in
 179 individual radiosonde profiles. The potential temperature gradient between 20 m and 50 m in each
 180 radiosonde profile were used to define six near-surface stability regimes. Above 20 m, the potentially
 181 warm temperatures usually present in radiosonde profiles is avoided (Schwartz and Doswell, 1991;
 182 Mahesh et al., 1997), while still being representative of the near-surface stability. These six near-surface
 183 stability regimes range from near neutral conditions (NN; $d\theta/dz < 0.5 \text{ K (100 m)}^{-1}$) to extremely strongly



184 stable conditions (ESS; $d\theta/dz > 30 \text{ K (100 m)}^{-1}$). Thresholds to distinguish between these six regimes,
185 near neutral (NN), weak stability (WS), moderate stability (MS), strong stability (SS), very strong
186 stability (VSS) and extremely strong stability (ESS) were defined by Dice et al. (2023) and Jozef et al.
187 (2023) (Table 2), and were found to have robust applications in both the Antarctic and Arctic.

188 Stability regimes aloft were also defined, as many of the radiosonde profiles have enhanced
189 stability above layers of weaker, near-surface stability. Stability aloft was defined by first finding the top
190 of the boundary layer based on the bulk Richardson number, as described in Jozef et al. (2022). A ratio
191 between the production or suppression of turbulence by buoyancy and turbulence generated by wind
192 shear, the bulk Richardson number is used to identify the point in each radiosonde profile where turbulence
193 is no longer sustained (Stull, 1988). Thus, the height of the boundary layer is given by the height at which
194 the bulk Richardson number exceeds the critical value (0.5) and remains above this value for at least 20
195 consecutive meters in each radiosonde profile. Then, the stability regime above the boundary layer was
196 found by identifying the maximum potential temperature gradient between the top of the boundary layer
197 and 500 m (the top of the profile used in this study), using the same potential temperature gradient
198 thresholds used to define the near-surface stability (Table 2). An aloft stability regime was only attributed
199 to a radiosonde profile when stability aloft was greater than the near-surface stability. In cases where the
200 greatest stability in the profile occurs near the surface, no aloft stability regime is defined.

201 It was also noted in the near neutral (NN) and weak stability (WS) regimes that there was one
202 grouping of profiles where the boundary layer depth is greater than 125 m, and one grouping where the
203 depth was less than 125 m. For these profiles with a boundary layer depth less than 125 m and a NN or
204 WS stability designation, the regime was instead identified to be very-shallow mixed, or VSM.

205 The near-surface and aloft stability (if applicable) for each radiosonde profile were combined to
206 give the final stability regime. Thus, profiles with, for example, near-neutral stability near the surface and
207 moderate stability above the boundary layer was named as “near-neutral, moderate stability aloft”, or
208 “NN-MSA”. Applying this method to the various combinations of near-surface and aloft stability regimes
209 left seven “stability groupings”, where the near-surface stability is the same, but varied stability is present
210 aloft. For example, the NN “stability grouping” consists of the following NN (near-neutral), NN-WSA
211 (near-neutral, weak stability aloft), NN-MSA (near-neutral, moderate stability aloft), and NN-SSA (near-
212 neutral, strong stability aloft). Figures throughout this paper use distinct colors for each of these stability
213 groupings: NN, brown, VSM, red, WS, green, MS, blue, SS, purple, VSS, pink, and ESS, indigo. The
214 darkest color in each group is the “basic near-surface stability regime”, where no enhanced stability aloft
215 is present, and the color used to represent the regimes decreases in intensity as stability aloft in each
216 grouping increases. The basic near-surface stability regimes consist of the following: NN, WS, MS, SS,
217 VSS, and ESS, as well as VSM-WSA. The VSM-WSA regime is also considered a basic near-surface
218 stability regime because the VSM portion of this regime is a subset from the NN or WS regime, as it has
219 the same potential temperature gradient, just a shallower boundary layer (Dice et al., 2023). Additionally,
220 to help with visualization of the vertical structure of the regimes, an example profile of the potential
221 temperature gradient and potential temperature anomaly for each of the twenty boundary layer regimes
222 can be seen in Figure 2.



223 *Table 2: As seen in Dice et al. (2023): Boundary Layer Regime definition scheme. The left column of the*
 224 *table shows the potential temperature gradient ($d\theta/dz$ in $K (100 m)^{-1}$) thresholds used to define each of*
 225 *the six basic near-surface stability regimes from 20 m to 50 m. The middle column shows how the very*
 226 *shallow mixed layer definition was applied to NN and WS cases. The third column shows the maximum*
 227 *potential temperature gradient thresholds ($d\theta/dz$ in $K (100 m)^{-1}$) for the aloft stability regimes.*

Near-Surface Stability	Very Shallow Mixed Layer	Stability Above Boundary Layer ("Aloft")
Near-Neutral (NN): $d\theta dz^{-1} < 0.5 K (100 m)^{-1}$	If near-surface stability = NN or WS and ABL height <125 m ➤ Near-surface stability = Very-Shallow Mixed (VSM)	
Weak Stability (WS): $d\theta dz^{-1} \geq 0.5 K (100 m)^{-1}$ and < 1.75 $K (100 m)^{-1}$		Weak Stability Aloft (-WSA): $d\theta dz^{-1} \geq 0.5 K (100 m)^{-1}$ and < 1.75 $K (100 m)^{-1}$
Moderate Stability (MS): $d\theta dz^{-1} \geq 1.75 K (100 m)^{-1}$ and < 5 $K (100 m)^{-1}$		Moderate Stability Aloft (-MSA): $d\theta dz^{-1} \geq 1.75 K (100 m)^{-1}$ and < 5 $K (100 m)^{-1}$
Strong Stability (SS): $d\theta dz^{-1} \geq 5 K (100 m)^{-1}$ and < 15 $K (100 m)^{-1}$		Strong Stability Aloft (-SSA): $d\theta dz^{-1} \geq 5 K (100 m)^{-1}$
Very Strong Stability (VSS): $d\theta dz^{-1} \geq 15 K (100 m)^{-1}$ and < 30 $K (100 m)^{-1}$		Very Strong Stability Aloft (-VSSA): $d\theta dz^{-1} \geq 15 K (100 m)^{-1}$
Extremely Strong Stability (ESS): $d\theta dz^{-1} \geq 30 K (100 m)^{-1}$		Extremely Strong Stability Aloft (-ESSA): $d\theta dz^{-1} \geq 30 K (100 m)^{-1}$

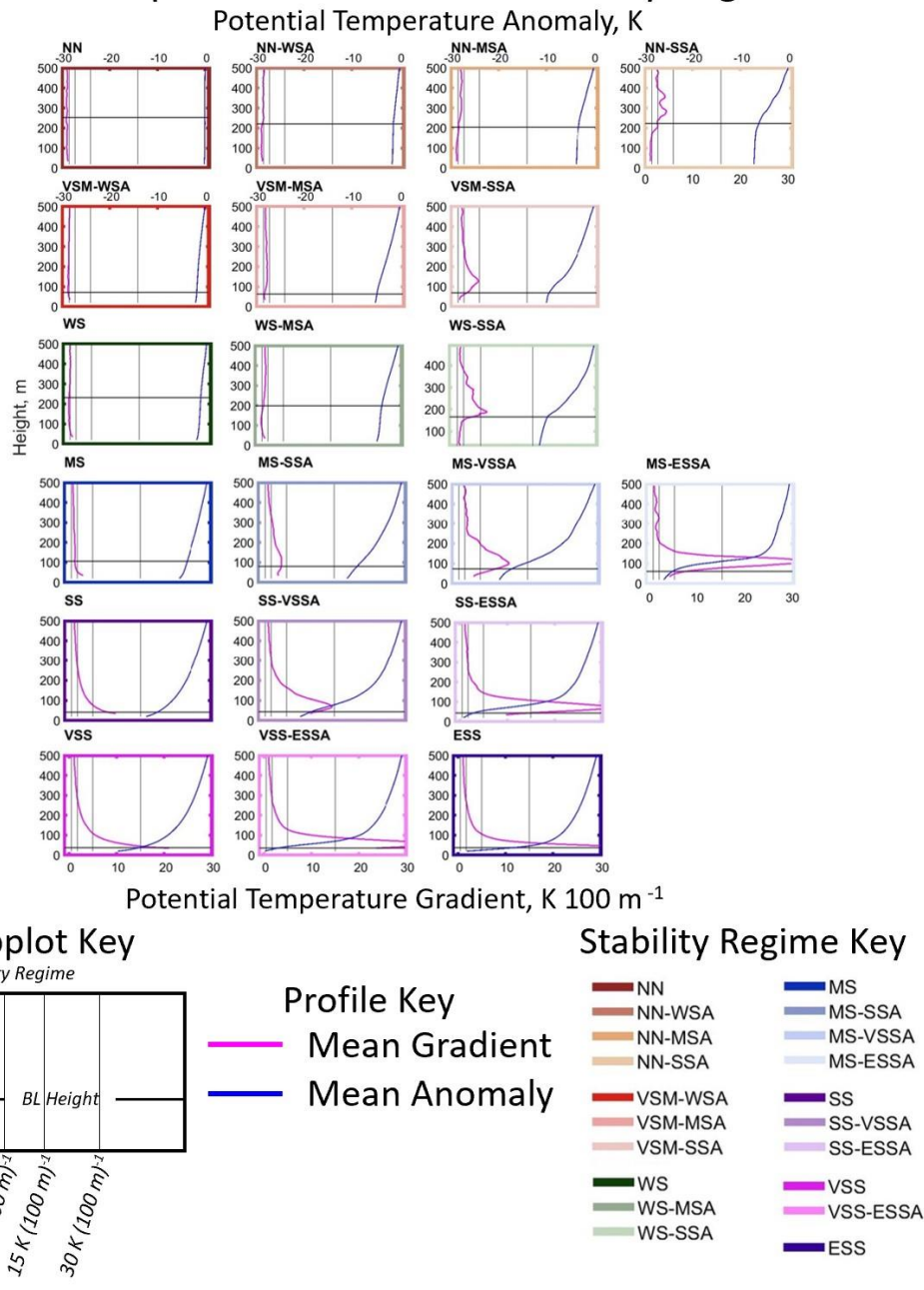


228 *Table 3: As seen in Dice et al. (2023): Boundary Layer Regime acronyms and color codes. On the left is*
 229 *the color and acronym used to represent each of the 20 stability regimes in figures and tables throughout*
 230 *this paper, and the full regime name is spelled out on the right. The basic near-surface stability regimes*
 231 *are denoted in bold font.*

Regime Color and Acronym	Regime Full Name
NN	Near Neutral
NN-WSA	Near Neutral- Weak Stability Aloft
NN-MSA	Near Neutral- Moderate Stability Aloft
NN-SSA	Near Neutral- Strong Stability Aloft
VSM-WSA	Very Shallow Mixed- Weak Stability Aloft
VSM-MSA	Very Shallow Mixed- Moderate Stability Aloft
VSM-SSA	Very Shallow Mixed- Strong Stability Aloft
WS	Weak Stability
WS-MSA	Weak Stability- Moderate Stability Aloft
WS-SSA	Weak Stability- Strong Stability Aloft
MS	Moderate Stability
MS-SSA	Moderate Stability- Strong Stability Aloft
MS-VSSA	Moderate Stability- Very Strong Stability Aloft
MS-ESSA	Moderate Stability- Extremely Strong Stability Aloft
SS	Strong Stability
SS-VSSA	Strong Stability- Very Strong Stability Aloft
SS-ESSA	Strong Stability- Extremely Strong Stability Aloft
VSS	Very Strong Stability
VSS-ESSA	Very Strong Stability- Extremely Strong Stability Aloft
ESS	Extremely Strong Stability



Example Profiles for Each Stability Regime



232 Figure 2: Examples of the vertical profile structure of the regimes listed in Table 3. The potential
 233 temperature gradient is shown in pink (top axis), the potential temperature anomaly is shown in blue
 234 (bottom axis). The stability regime acronym is given above the top left corner of each subplot and is also
 235 indicated by the colored outline around each plot, according to the key in the bottom right of the figure.



236 3 Results

237 Once each radiosonde profile has been assigned a boundary layer stability regime, the list of dates
238 and times when each regime occurred is used to calculate statistics of the boundary layer forcing
239 mechanisms for each regime. To assess the possible atmospheric forcing that drives the variability in
240 stability regimes we compare downwelling longwave radiation and 20 m wind speed across the different
241 stability regimes (Table 2). The 20 m radiosonde wind speed is used rather than the surface wind speed to
242 remove any potential discrepancy in wind speeds due to the difference in location of surface observations
243 and radiosonde launch sites, as described in Section 2.1. These two forcing variables serve as proxies for
244 varying surface energy fluxes and mechanical mixing which may lead to variations in near-surface
245 stability (Rodrigo and Anderson, 2013). As observed in Dice and Cassano (2022) and other studies,
246 surface heating or reduced cooling (increased downward radiative fluxes) and increased mechanical
247 mixing (greater near surface wind speed and shear) lead to weaker stability, while surface cooling and
248 decreased mechanical mixing allow stable conditions and temperature inversions to form at the surface
249 (e.g., King and Turner, 1997; Andreas et al., 2000; Hudson and Brandt, 2005).

250 Box plots of downwelling longwave radiation and 20 m radiosonde wind speed are shown for
251 each stability regime with increasing stability, from NN to ESS, from left to right on an annual (left panel)
252 and seasonal (right four panels) basis at each site (Figures 3 through 12). The seasons are defined in this
253 study as follows: summer (DJ), fall (FMA), winter (MJJA), and spring (SON), as used in previous studies
254 of the Antarctic (Cassano et al., 2016, Seefeldt and Cassano, 2012). Each box plot shows the mean (black
255 asterisk), median (black horizontal line), 25th and 75th percentiles (edges of box), and 10th and 90th
256 percentiles (whiskers) for each regime, although the analysis below will primarily focus on the mean
257 values. The number of observations in each regime annually and seasonally are given by the numbers at
258 the top of each plot, and the horizontal black line across each of the annual and seasonal panels is the
259 mean for that period of time. Regimes with fewer than 10 observations will not be discussed at length, as
260 these small sample sizes may not be representative. The number of observations, mean downwelling
261 longwave radiation, and mean 20 m wind speed in each regime are listed in Tables S1 to S5 for each site.

262 3.1 South Pole

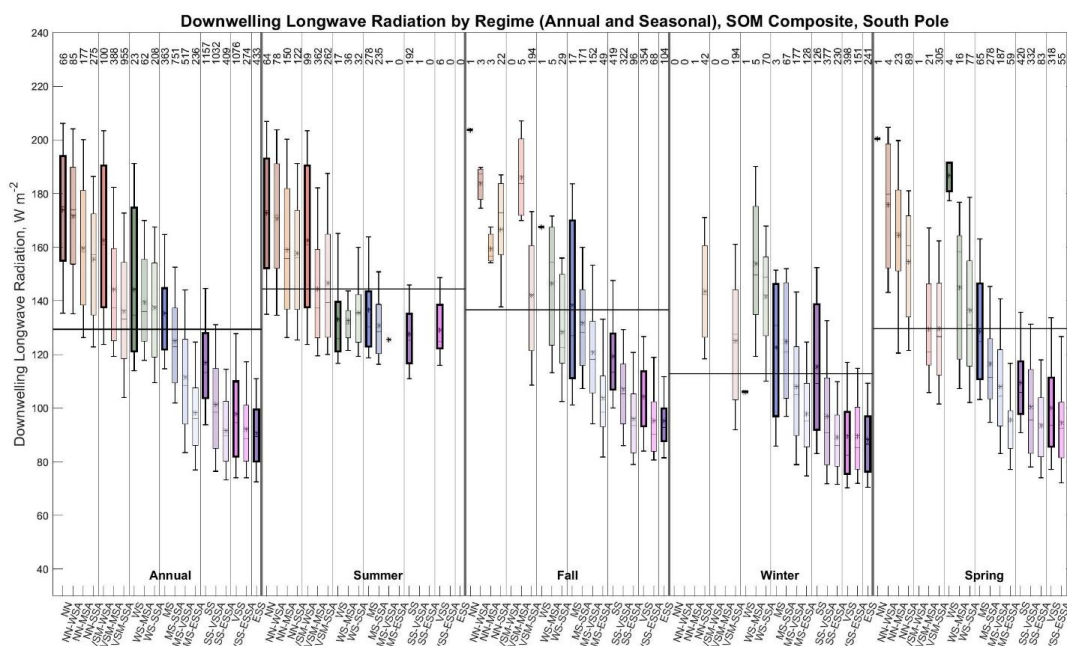
263 South Pole, a high-plateau continental interior site, is generally characterized by strong and
264 persistent radiative cooling allowing for the formation of strong stability (Stone and Kahl, 1991; Lazzara
265 et al., 2012). Dice et al. (2023) noted that boundary layer stability at South Pole was largely dominated by
266 the SS, VSS, or ESS regimes, occurring near the surface 51% of the year. However, they found when
267 considering the maximum stability in the profile, SS, VSS, or ESS conditions occur 85.2% of the year,
268 either near the surface or aloft but below 500 m. Here, the radiative forcing and mechanical mixing for
269 each stability regime will be analyzed on an annual and seasonal basis.

270 The downwelling longwave radiation for each regime annually and seasonally is shown in Figure
271 3 and Table S1. Considering changes in downwelling longwave radiation as stability increases, the first
272 result to note is that annually, the downwelling longwave radiation (Figure 3) decreases by nearly half
273 from weak to strong stability across the basic near-surface stability regimes from NN (174 W m^{-2}) to ESS
274 (91 W m^{-2}). Similarly, in the fall and spring, downwelling longwave radiation consistently decreases from
275 the MS (138 W m^{-2} in the fall 129 W m^{-2} in the spring) to ESS (95 W m^{-2} in the fall and 93 W m^{-2} in the
276 spring) basic near-surface stability regimes, which are the most common regimes in these seasons. In the
277 winter downwelling longwave radiation is higher in the SS (115 W m^{-2}) regime, compared to the much
278 lower values in the VSS (90 W m^{-2}) and ESS (88 W m^{-2}) regimes, indicating a clear difference in forcing
279 for relatively weaker versus relatively stronger stability regimes. A similar observation is noted in the



280 summer, where the downwelling longwave radiation is similar in the NN (173 W m⁻²) and VSM-WSA
 281 (163 W m⁻²) regimes and is then about 21% lower, and similar, across the WS, MS, and SS regimes,
 282 ranging from 128 to 137 W m⁻². Annually and across all seasons, the downwelling longwave radiation in
 283 the SS, VSS, and ESS regimes is almost always lower than the seasonal mean, and the downwelling
 284 longwave radiation in the NN regime, and usually in the VSM regime, is above the seasonal mean.

285 When stability aloft increases within a given stability grouping, downwelling longwave radiation
 286 usually decreases. In the fall, winter, and spring, and on an annual basis, this decrease is largest in the MS
 287 stability grouping, by as much as 26 W m⁻² to 37 W m⁻², followed by the decrease in the SS stability
 288 grouping, by as much as 16 W m⁻² to 26 W m⁻². In the summer, downwelling longwave radiation
 289 decreases within the NN (15 W m⁻²), VSM (16 W m⁻²), and MS (6 W m⁻²) stability groupings, although
 290 not as strongly as what was seen within stability groupings in the other seasons, while downwelling
 291 longwave radiation is more similar as stability aloft increases in the WS stability grouping.



292 *Figure 3: Box plot showing the distribution of downwelling longwave radiation observed for each stability regime at*
 293 *South Pole annually (left panel) and seasonally (right four panels – summer, fall, winter, and spring). Box plots*
 294 *show median downwelling longwave radiation (horizontal line), mean downwelling longwave radiation (black star),*
 295 *25th and 75th percentiles (edges of boxes), and 10th and 90th percentiles (whiskers). The thin vertical black lines in*
 296 *the figure separate the stability groupings in each panel (annual or seasonal). The thin horizontal black lines across*
 297 *each panel (annual or seasonal), indicate the mean value for that entire time period. The numbers at the top indicate*
 298 *the number of radiosonde profiles in each regime.*

299 While the trend in downwelling longwave radiation both annually and seasonally generally shows
 300 a clear decrease from weak to strong stability both at the surface and aloft (Figure 3 and Table S1), the 20
 301 m wind speed (Figure 4; Table S1) observations for the various regimes shows less of a clear difference in
 302 wind speed with varying stability. However, it is noted that for most near-surface stability groupings the
 303 20 m wind speed tends to increase with increasing stability aloft, suggesting that increased mechanical



304 mixing by stronger winds is required for maintaining reduced near-surface stability as stability aloft
305 increases, consistent with Dice and Cassano (2022).

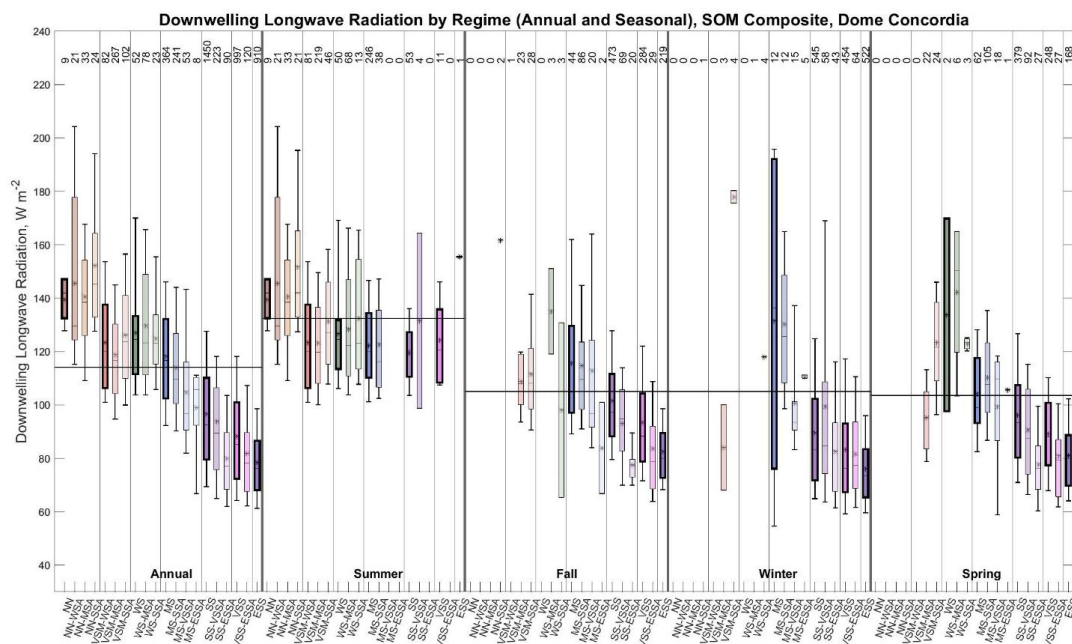
306 When looking at just the basic near-surface stability regimes on an annual basis mean wind
307 speeds are highest in the WS regime (6.2 m s^{-1}), and then lower and similar across the SS, VSS, and ESS
308 regimes, ranging from 5.1 m s^{-1} to 5.4 m s^{-1} , and lowest in the NN, VSM-WSA, and MS regimes, ranging
309 from 4.3 m s^{-1} to 4.5 m s^{-1} . A similar pattern is observed in the summer, where wind speeds are the
310 strongest in the WS regime (5.7 m s^{-1}), weaker in the NN (4.5 m s^{-1}) and the VSM-WSA (4.3 m s^{-1})
311 regimes and weakest in the MS (3.9 m s^{-1}) and SS regimes (3.7 m s^{-1}). Annually and in the summer, the
312 stronger wind speeds in the WS regime in comparison to the VSM-WSA regime is a key difference that
313 distinguishes these regimes which are similar in boundary layer strength (Table 2) but have different
314 boundary layer depths. This will be discussed further in the discussion section below. In the fall and
315 spring, wind speed is slightly higher in the MS regime (6.0 m s^{-1} in the fall and 5.8 m s^{-2}), and weaker and
316 similar across the SS, VSS and ESS regimes (between 4.7 m s^{-1} and 5.2 m s^{-1} in the fall and between 5.0
317 m s^{-1} and 5.2 m s^{-2} in the spring). In the winter, wind speeds decrease from SS (7.1 m s^{-1}) to ESS (5.3 m s^{-1}),
318 which is a more consistent decrease with increasing stability, and more like the expected result that
319 weaker winds are associated with stronger stability (e.g., Cassano et al., 2016).

320 Winds generally increase with increasing stability aloft in each stability grouping annually and, in
321 the fall and spring (Figure 4; Table S1). Annually, the wind speed increases the most in the MS stability
322 grouping from 4.4 m s^{-1} to 8.5 m s^{-1} , but also shows clear increases across the NN, VSM, WS, SS, and
323 VSS stability groups. Wind speed increases 1.3 m s^{-1} to 2.8 m s^{-1} with increasing stability in the
324 frequently observed MS, SS, and VSS stability groups in the fall and spring. In contrast, in the winter, as
325 stability aloft increases within stability groupings, wind speed increases only slightly with increasing
326 stability aloft in the SS (0.6 m s^{-1}) and VSS (0.5 m s^{-1}) stability groupings. In comparison, wind speeds
327 across the MS-SSA, MS-VSSA, and MS-ESSA regimes do not follow a very clear trend, ranging from
328 8.5 m s^{-1} to 8.9 m s^{-1} . Similarly in the summer, wind speed increases 0.6 m s^{-1} to 0.9 m s^{-1} in the NN,
329 VSM, and WS stability groupings as stability aloft increases. It is also interesting to note that the mean
330 wind speed for the basic near-surface stability regimes, annually and seasonally, is generally lower than
331 the annual or seasonal mean, while the wind speeds in regimes with enhanced stability aloft is often
332 higher than the annual or seasonal mean. As noted above, this suggests that stronger mechanical mixing
333 may be needed to reduce near-surface stability in the presence of enhanced stability aloft, which was also
334 noted by Dice and Cassano (2022) at McMurdo.



360 annual or seasonal means in MS or weaker stability regimes. In summer, there is little change in
 361 downwelling longwave radiation across the most frequently observed basic-near surface stability regimes
 362 (VSM-WSA to VSS) ranging from 120 W m⁻² to 127 W m⁻².

363 Changes in downwelling longwave radiation within regime groups, as aloft stability increases, is
 364 not always as clear as was seen for the near-surface stability regimes (Figure 5; Table S2). On an annual
 365 basis there is little change in downwelling longwave radiation within the NN, VSM, or WS stability
 366 groups but there is a consistent decrease in downwelling longwave radiation as aloft stability increases in
 367 the MS, SS, and VSS stability groups. In fall and spring, downwelling longwave radiation also
 368 consistently decreases in the SS and VSS stability groups, and slightly decreases from MS to MS-VSSA
 369 in the fall. In the winter, downwelling longwave radiation decreases from MS to MS-VSSA. In some
 370 cases, there is little change within regime groups (e.g., SS and VSS in winter, and MS in the fall and
 371 spring, excluding MS-ESSA) while in other cases there is only a noticeable decrease in downwelling
 372 longwave radiation for the strongest aloft stability within a regime group (e.g., SS in fall and SS and VSS
 373 in spring). In the summer there is little change in downwelling longwave radiation as stability aloft
 374 increases within the various stability regime groups.



375 *Figure 5: Box plot showing the distribution of downwelling longwave radiation observed for each stability regime at*
 376 *Dome C annually (left panel) and seasonally (right four panels – summer, fall, winter, and spring). Box plots show*
 377 *median downwelling longwave radiation (horizontal line), mean downwelling longwave radiation (black star), 25th*
 378 *and 75th percentiles (edges of boxes), and 10th and 90th percentiles (whiskers). The thin vertical black lines in the*
 379 *figure separate the stability groupings in each panel (annual or seasonal). The thin horizontal black lines across*
 380 *each panel (annual or seasonal), indicate the mean value for that entire time period. The numbers at the top indicate*
 381 *the number of radiosonde profiles in each regime.*

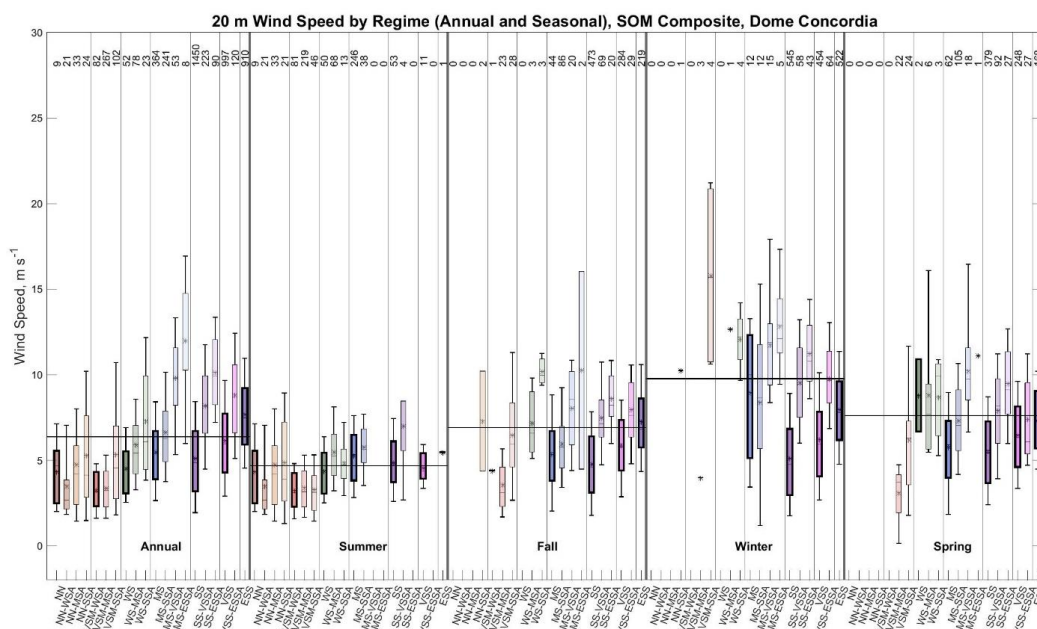
382 The distribution of 20 m wind speed for each stability regime, on an annual and seasonal basis, is
 383 shown in Figure 6 and Table S2. Interestingly, wind speed generally increases with increasing stability



384 annually and in the fall, winter, and spring, which is unexpected. Another robust feature seen in Figure 6
385 is that 20 m wind speed generally increases within regime groups as aloft stability increases, such that
386 mean wind speed for the regimes with enhanced stability aloft is often above the annual or seasonal mean,
387 while mean wind speeds for the basic near-surface stability regimes are below or close to the annual or
388 seasonal mean.

389 Considering first the basic near-surface stability regimes, a surprising result is seen for the annual
390 data. The 20 m wind speed increases by almost 80% from the weakest stability, VSM-WSA (3.3 m s^{-1}) to
391 the strongest stability, ESS (7.7 m s^{-1}). As discussed in the introduction, stronger winds are typically
392 associated with weaker near-surface stability (e.g., Pietroni et al., 2013; Cassano et al., 2016), thus, this is
393 a surprising result, which will be discussed further in Section 4. In the winter, for the basic near-surface
394 stability regimes with the most observations, the wind speed is highest in the MS regime (9.0 m s^{-1}),
395 decreases to SS (5.1 m s^{-1}), and then increases to ESS (8.0 m s^{-1}). In the fall and spring, the MS (5.3 m s^{-1}
396 in the fall and 5.8 m s^{-1} in the spring) and SS (4.8 m s^{-1} in the fall and 5.5 m s^{-1} in the spring) regimes have
397 similar wind speeds that are below the seasonal mean, while the wind speed is higher in and increases
398 from VSS (5.9 m s^{-1} in the fall and 6.5 m s^{-1} in the spring) to ESS (7.3 m s^{-1} in both seasons). Unlike what
399 was seen for the annual data, differences in the 20 m wind speed across the basic near-surface stability
400 regimes in the summer do not show a consistent pattern as stability varies. The 20 m wind speed is
401 weakest for the VSM-WSA regime (3.2 m s^{-1}), almost 40% stronger and similar for the WS (4.3 m s^{-1}),
402 VSS (4.6 m s^{-1}), and SS (4.8 m s^{-1}) regimes and strongest for the MS (5.3 m s^{-1}) regime. The weaker
403 winds in the VSM-WSA regime in comparison to those in the WS regime will be discussed in detail in
404 Section 4.

405 When looking at wind speed variability within stability groups as stability aloft increases there is a
406 relatively consistent pattern of stronger winds being associated with increasing stability aloft. This is very
407 clearly seen in the annual data in Figure 6 and Table S2. Here, the wind speed change is largest in the SS
408 regime group, increasing from 5.1 m s^{-1} to 10.1 m s^{-1} , and in MS regime group, increasing from 5.5 m s^{-1}
409 to 9.8 m s^{-1} . Smaller increases in wind speed, of 1.8 m s^{-1} to 2.8 m s^{-1} , are seen across the NN, VSM, WS,
410 and VSS regime groups annually. Clear increases in wind speed with increasing stability aloft are seen
411 for the MS, SS and VSS regime groups in fall, winter, and spring. The largest increase in wind speed
412 occurs in the SS regime in the winter (increase of 6.1 m s^{-1}) and fall (3.8 m s^{-1}) and in the MS regime in
413 the spring (increase of 4.4 m s^{-1}). In the summer, speeds weakly increase in the NN, WS and MS regimes
414 (0.5 m s^{-1} to 1.4 m s^{-1}) and show little change for the other regime groups. In most cases the mean wind
415 speed in each regime is less than the annual or seasonal mean for the basic near-surface stability regimes
416 and increases to greater than the annual or seasonal mean for many of the enhanced stability aloft
417 regimes. This suggests that to maintain a given near-surface stability stronger winds, and mechanical
418 mixing, is required as stability aloft increases. This behavior is consistent with findings of Cassano et al.
419 (2016), Dice and Cassano (2022) and others that found that stronger winds typically reduce near surface
420 stability.



421 *Figure 6: Box plot showing the distribution of 20 m wind speed observed for each stability regime at Dome C*
 422 *annually (left panel) and seasonally (right four panels – summer, fall, winter, and spring). Box plots show median*
 423 *20 m wind speed (horizontal line), mean 20 m wind speed (center black star), 25th and 75th percentiles (edges of*
 424 *boxes), and 10th and 90th percentiles (whiskers). The thin vertical black lines in the figure separate the stability*
 425 *groupings in each panel (annual or seasonal). The thin horizontal black lines across each panel (annual or*
 426 *seasonal), indicate the mean value for that entire time period. The numbers at the top indicate the number of*
 427 *radiosonde profiles in each regime.*

428 3.3 McMurdo

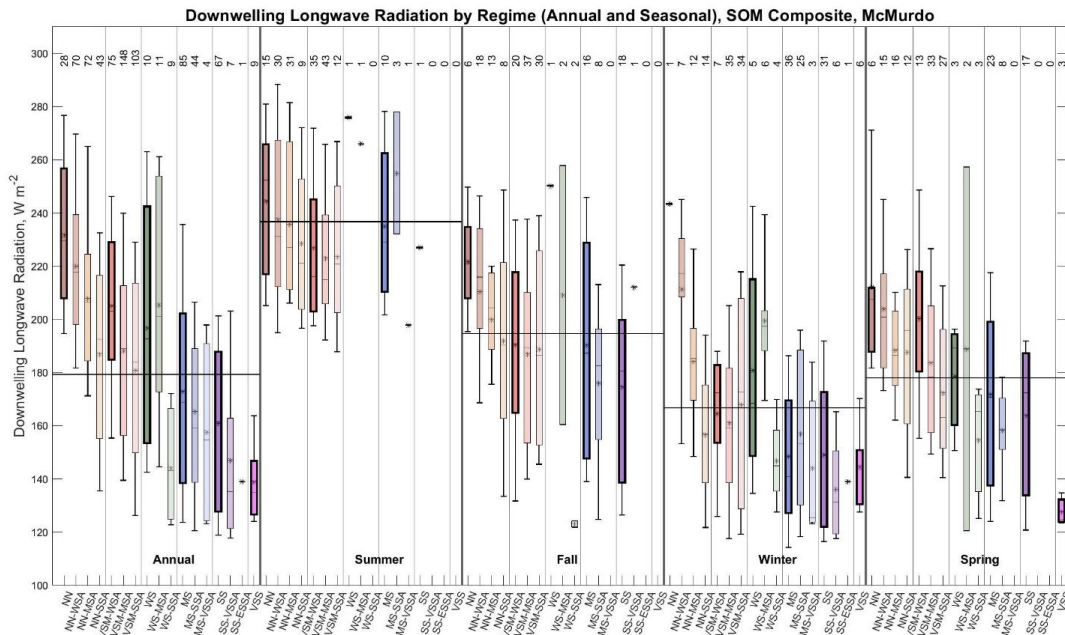
429 The results at the two continental interior sites above are reflective of the nearly constant,
 430 strongly stable conditions seen in the boundary layer throughout much of the year there, that form in
 431 response to the extremely low values of downwelling longwave radiation (Phillpot and Zillman, 1970;
 432 Zhang, et al., 2011; Dice et al., 2023). Now, the three coastal sites will be analyzed: McMurdo,
 433 Neumayer, and Syowa. In comparison to the continental interior sites, a wider range of boundary layer
 434 stability regimes are present at these sites (Dice et al., 2023), and are expected to have more complex
 435 forcing mechanisms, such as temperature advection (Dice and Cassano, 2022), katabatic winds
 436 (Murakoshi, 1958; Hudson and Brandt, 2005; Lazzara et al., 2012), and cyclonic activity (Silva et al.,
 437 2022). Specifically at McMurdo, Dice et al. (2023) found that the summer was largely dominated by the
 438 NN, VSM, and WS regimes (92.1%), while near surface stability in the winter was more varied but found
 439 that MS or SS conditions occur near the surface or aloft 84.6% of the winter season.

440 The downwelling longwave radiation at McMurdo as a function of stability regime is shown
 441 annually and seasonally in Figure 7 and Table S3. Most notably, the downwelling longwave radiation
 442 shows a clear decrease from weak to strong stability across the basic near-surface stability regimes
 443 annually and in the transition seasons. On an annual basis downwelling longwave radiation decreases by
 444 over 70 W m^{-2} from NN (232 W m^{-2}) to SS (161 W m^{-2}). In the transition seasons, the decrease from
 445 weakest to strongest stability is between 16 W m^{-2} and 36 W m^{-2} , from VSM-WSA (191 W m^{-2} in the fall



446 and 200 W m^{-2} in the spring) to SS (175 W m^{-2} in the fall and 164 W m^{-2} in the spring). There is not a
 447 consistent decrease in downwelling longwave radiation with increasing basic near-surface stability in the
 448 summer and winter for the most frequently observed regimes. In the summer, downwelling longwave
 449 radiation is highest in the NN basic near-surface stability regime (244 W m^{-2}), slightly less in the MS
 450 regime (235 W m^{-2}) and lowest in the VSM-WSA regime (227 W m^{-2}). In the winter, downwelling
 451 longwave radiation is about the same in the MS regime (148 W m^{-2}) and the SS regime (149 W m^{-2}).
 452 Generally, across all seasons and annually, regimes with stability MS and stronger have downwelling
 453 longwave radiation below the seasonal mean (Figure 7). These results are consistent with those found by
 454 Dice and Cassano (2022) at McMurdo Station, where decreasing downwelling longwave radiation with
 455 increasing stability was observed annually and seasonally, with the highest values observed in summer,
 456 and lowest in winter.

457 When considering stability aloft, downwelling longwave radiation usually decreases with
 458 increasing stability aloft (Figure 7; Table S3). Annually, downwelling longwave radiation decreases
 459 within the NN (45 W m^{-2} difference) and VSM (24 W m^{-2}) stability groups, and within the VSM stability
 460 group in the spring (28 W m^{-2}) and from NN-MSA to NN-SSA in the winter (27 W m^{-2}). In most of the
 461 other stability groupings in the other seasons, downwelling longwave radiation decreases only slightly as
 462 aloft stability increases (e.g. in the NN regime group in summer and fall) or does not show a uniform
 463 change as aloft stability increases (e.g. WS regime group in winter and spring).



464 *Figure 7: Box plot showing the distribution of downwelling longwave radiation observed for each stability regime at*
 465 *McMurdo annually (left panel) and seasonally (right four panels – summer, fall, winter, and spring). Box plots show*
 466 *median downwelling longwave radiation (horizontal line), mean downwelling longwave radiation (black star), 25th*
 467 *and 75th percentiles (edges of boxes), and 10th and 90th percentiles (whiskers). The thin vertical black lines in the*
 468 *figure separate the stability groupings in each panel (annual or seasonal). The thin horizontal black lines across*
 469 *each panel (annual or seasonal), indicate the mean value for that entire time period. The numbers at the top indicate*
 470 *the number of radiosonde profiles in each regime.*



471 Considering now the 20 m wind speed at McMurdo annually and seasonally (Figure 8; Table S3),
472 there is not a clear pattern across the basic near-surface stability regimes, but there is a tendency for wind
473 speed to increase with increasing stability aloft in many of the stability groups.

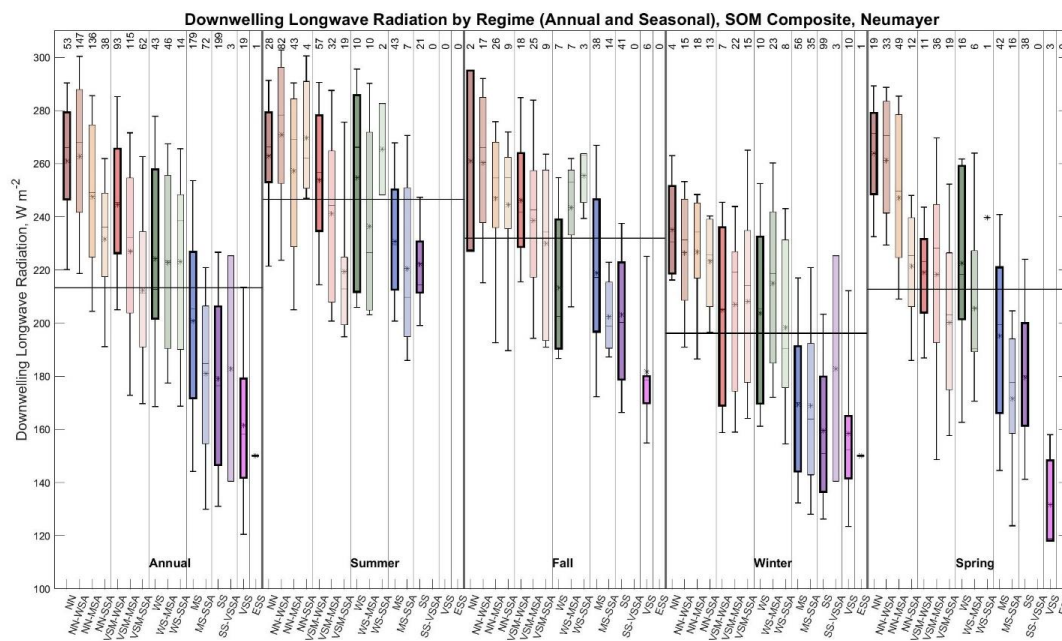
474 Annually, wind speed is greatest in the WS (5.3 m s^{-1}) and NN (5.2 m s^{-1}) basic near-surface
475 stability regimes. Wind speeds are more than 2 m s^{-1} lower and similar across the VSM-WSA, MS, and
476 SS regimes (2.5 m s^{-1} to 3.0 m s^{-1}). Similarly, in the summer the wind speed is highest in the NN regime
477 (5.4 m s^{-1}) and more than 3 m s^{-1} less in the VSM-WSA and MS regimes. The weaker winds in the VSM-
478 WSA regime, compared to either the NN or WS regimes will be discussed further in the next section.
479 Winds are similar between the frequently observed MS (1.9 m s^{-1}) and SS (2.0 m s^{-1}) regimes in winter. In
480 the fall similar winds occur between VSM-WSA (3.0 m s^{-1}) and MS (2.8 m s^{-1}), then increase from MS to
481 SS (5.3 m s^{-1}). In the spring, similar wind speeds also occur between VSM-WSA (3.1 m s^{-1}) and MS (3.3
482 m s^{-1}), but then decrease from MS to SS (2.4 m s^{-1}).

483 Wind speed increases with increasing stability aloft, for each stability grouping, on an annual
484 basis and usually in the seasons as well (Figure 8; Table S3). The largest change in wind speed with
485 increased stability aloft occurs in the fall. At this time of year wind speeds within the NN and VSM
486 regimes increase by over half between the basic near-surface stability regime and the strongest aloft
487 stability regime (3.9 m s^{-1} to 6.5 m s^{-1} from NN-WSA to NN-MSA and 3.0 m s^{-1} to 7.1 m s^{-1} in the VSM
488 stability grouping). Wind speed also generally increases with increasing stability aloft within each
489 stability group for the other seasons, but usually by less than 2 m s^{-1} , and often closer to 1 m s^{-1} . This
490 tendency for wind speed to increase with increasing stability aloft was also noted at both the continental
491 interior sites above and may reflect the need for stronger winds to weaken the near surface stability when
492 stronger stability aloft is present. The exceptions to this are decreases, rather than increases, in wind speed
493 of 1 to 2 m s^{-1} with increasing aloft stability in the NN stability group in the winter (NN-MSA to NN-
494 SSA; a decrease of 1.1 m s^{-1}) and spring (NN-WSA to NN-SSA; a decrease of 0.6 m s^{-1}).



519 fundamental differences in radiative forcing between weaker and stronger stability regimes in these
520 seasons.

521 A comparison of downwelling longwave radiation across stability regimes can also be made as
522 stability aloft increases within a given stability regime grouping. The most noteworthy observation is the
523 very strong decrease within stability groupings as stability aloft increases in the spring where
524 downwelling longwave radiation decreases by as much as 42 W m⁻² in the NN stability grouping and 23
525 W m⁻² in the MS stability grouping. A weaker decrease is observed in the fall for the MS (16 W m⁻²) and
526 VSM (7 W m⁻²) stability groups. In the summer, downwelling longwave radiation decreases with
527 increasing stability in the VSM and MS stability groupings, but not in the NN or WS groupings, where
528 downwelling longwave radiation is more varied. A similar observation is noted for the winter, where
529 downwelling longwave radiation slightly decreases in the NN stability grouping (excluding the basic
530 near-surface stability regime of NN), is nearly the same within the MS stability grouping, and increases or
531 is variable in all the other stability groupings.



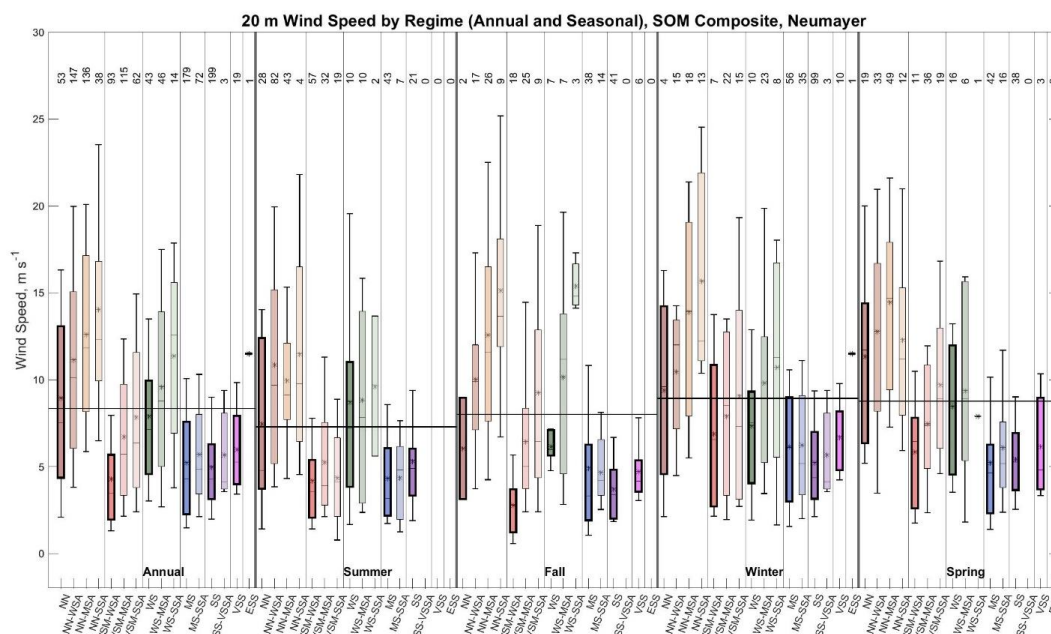
532 *Figure 9: Box plot showing the distribution of downwelling longwave radiation observed for each stability regime at*
533 *Neumayer annually (left panel) and seasonally (right four panels – summer, fall, winter, and spring). Box plots*
534 *show median downwelling longwave radiation (horizontal line), mean downwelling longwave radiation (black star),*
535 *25th and 75th percentiles (edges of boxes), and 10th and 90th percentiles (whiskers). The thin vertical black lines in*
536 *the figure separate the stability groupings in each panel (annual or seasonal). The thin horizontal black lines across*
537 *each panel (annual or seasonal), indicate the mean value for that entire time period. The numbers at the top indicate*
538 *the number of radiosonde profiles in each regime.*

539 The 20 m wind speed for each regime annually and seasonally is shown in Figure 10 and Table
540 S4. Annually wind speeds are highest in the NN (8.9 m s⁻¹) and WS (7.9 m s⁻¹) basic near-surface stability
541 regimes and lowest in VSM-WSA (4.3 m s⁻¹) regime. Wind speeds are similar in MS and SS (5.0 m s⁻¹ to
542 5.2 m s⁻¹) and slightly higher in the VSS (6.0 m s⁻¹) regime. The wind speed in the MS, SS and VSS
543 regimes are higher than those in the VSM-WSA regime but lower than those in the NN and WS regimes.



544 Similarly, in the summer and spring, wind speeds are highest in NN (7.4 m s^{-1} in the summer and 11.3 m
545 s^{-1} in the spring) and WS (8.7 m s^{-1} in the summer and 8.5 m s^{-1} in the spring), and lower and similar
546 across VSM-WSA, MS, and SS (4.2 m s^{-1} to 5.3 m s^{-1} in the summer and 5.2 m s^{-1} to 5.8 m s^{-1} in the
547 spring) regimes. In the winter, wind speeds decrease slightly from WS (7.3 m s^{-1}) to SS (5.2 m s^{-1}) and are
548 then slightly higher in VSS (6.7 m s^{-1}). In the fall, wind speeds are weakest in VSM-WSA (2.8 m s^{-1}), and
549 higher and decrease slightly from MS to SS (4.9 m s^{-1} to 3.7 m s^{-1}). It is also interesting to note here that
550 in most cases in all seasons the VSM-WSA, MS, SS and VSS basic near-surface stability regimes have
551 wind speeds lower than the seasonal mean, while the NN and WS regimes have mean winds speeds close
552 to or above the seasonal mean. This observation is consistent with Silva et al. (2022), who observed
553 weaker wind speeds with stronger stability at Neumayer. Winds in the VSM-WSA regime in comparison
554 to those in the NN and WS regimes are 49% weaker on an annual basis, and 41% to 47% weaker in the
555 summer and spring.

556 When considering stability aloft, another interesting result from Figure 10 and Table S4 is that
557 wind speed generally increases with increasing stability aloft in the stability groupings annually and
558 seasonally, although this is usually most evident in the NN, VSM and WS regime groups. As discussed
559 for other sites above, this may indicate that stronger mechanical mixing is necessary to reduce near-
560 surface stability. The increase in wind speed with increased stability aloft is largest in the NN regime in
561 the winter (5.2 m s^{-1}) and summer (2.5 m s^{-1}) and the VSM regime in the fall (3.6 m s^{-1}) and spring (3.9 m
562 s^{-1}). Additionally, regimes with enhanced stability aloft tend to have wind speeds above the seasonal mean,
563 especially in the NN and WS regime groupings, in comparison to the basic near-surface stability regimes.



564 *Figure 10: Box plot showing the distribution of 20 m wind speed observed for each stability regime at Neumayer*
 565 *annually (left panel) and seasonally (right four panels – summer, fall, winter, and spring). Box plots show median*
 566 *20 m wind speed (horizontal line), mean 20 m wind speed (center black star), 25th and 75th percentiles (edges of*
 567 *boxes), and 10th and 90th percentiles (whiskers). The thin vertical black lines in the figure separate the stability*
 568 *groupings in each panel (annual or seasonal). The thin horizontal black lines across each panel (annual or*
 569 *seasonal), indicate the mean value for that entire time period. The numbers at the top indicate the number of*
 570 *radiosonde profiles in each regime.*

571 3.5 Syowa

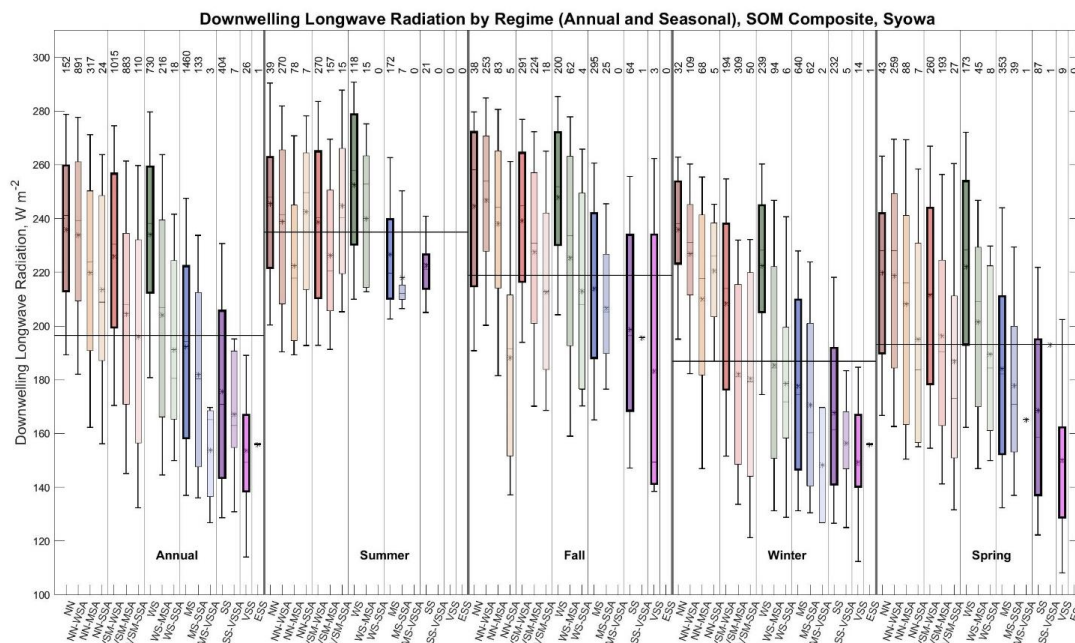
572 At Syowa, katabatic winds from the continental interior as well as passing cyclones both impact
 573 boundary layer conditions at this site (Murakoshi, 1958; Yamada and Hirasawa, 2018), resulting in
 574 potentially quickly changing stability. A variety of stability regimes are observed at this site (Dice et al.,
 575 2023), and like the other coastal sites, the summer is largely made up of the NN, VSM, and WS regimes
 576 (82.9%) near the surface. In the winter stronger stability either near the surface or aloft is generally
 577 present (71.1%).

578 Figure 11 and Table S5 shows the downwelling longwave radiation at Syowa for each regime
 579 annually and seasonally. The first thing to note about the downwelling longwave radiation at Syowa is
 580 that the NN, VSM-WSA, and WS basic near-surface stability regimes have similar and larger
 581 downwelling longwave radiation than the MS and stronger stability regimes annually and for each season.
 582 On an annual basis, mean downwelling longwave radiation varies from 226 W m⁻² to 236 W m⁻² across
 583 the NN, VSM-WSA, and WS regimes and then steadily decreases from WS (234 W m⁻²) to VSS (154 W
 584 m⁻²). In the winter and spring, this pattern is the strongest, with downwelling longwave radiation ranging
 585 from 208 W m⁻² to 236 W m⁻² across the NN, VSM-WSA, and WS regimes. It is then about 44 W m⁻²
 586 lower in MS (178 W m⁻² to 184 W m⁻²), SS (168 W m⁻² to 169 W m⁻²), and VSS (150 W m⁻²). This pattern
 587 is weaker but still present in the summer and fall, with downwelling longwave radiation ranging from 239
 588 W m⁻² to 253 W m⁻² across NN, VSM-WSA, and WS in the summer. It is then approximately 26 W m⁻² to



589 34 W m⁻² lower in MS (214 W m⁻² to 227 W m⁻²) and SS (199 W m⁻² to 223 W m⁻²). Annually and
 590 seasonally, downwelling longwave radiation in the NN, VSM-WSA, and WS basic near-surface stability
 591 regimes is usually above the seasonal mean while the downwelling longwave radiation in the MS, SS, and
 592 VSS regimes is usually below the seasonal mean. This suggests distinct radiative forcing for the most
 593 stable basic near-surface stability regimes (MS and stronger) compared to the three weakest regimes (NN,
 594 VSM-WSA, and WS) annually and seasonally at Syowa.

595 When considering stability aloft in each stability grouping, generally downwelling longwave
 596 radiation decreases as stability aloft increases for most regimes and seasons (Figure 11, Table S5). The
 597 strongest decrease in downwelling longwave radiation occurs in the winter in the WS regime, a decrease
 598 of 36 W m⁻². In the summer, the largest change occurs in the NN regime, with a decrease of 22 W m⁻²,
 599 and to a lesser extent in the WS regime, a decrease of 13 W m⁻². In the transition seasons, there is also a
 600 strong decrease in downwelling longwave radiation especially from VSM-WSA (239 W m⁻² in the fall and
 601 212 W m⁻² in the spring) to VSM-SSA (213 W m⁻² in the fall and 187 W m⁻² in the spring).



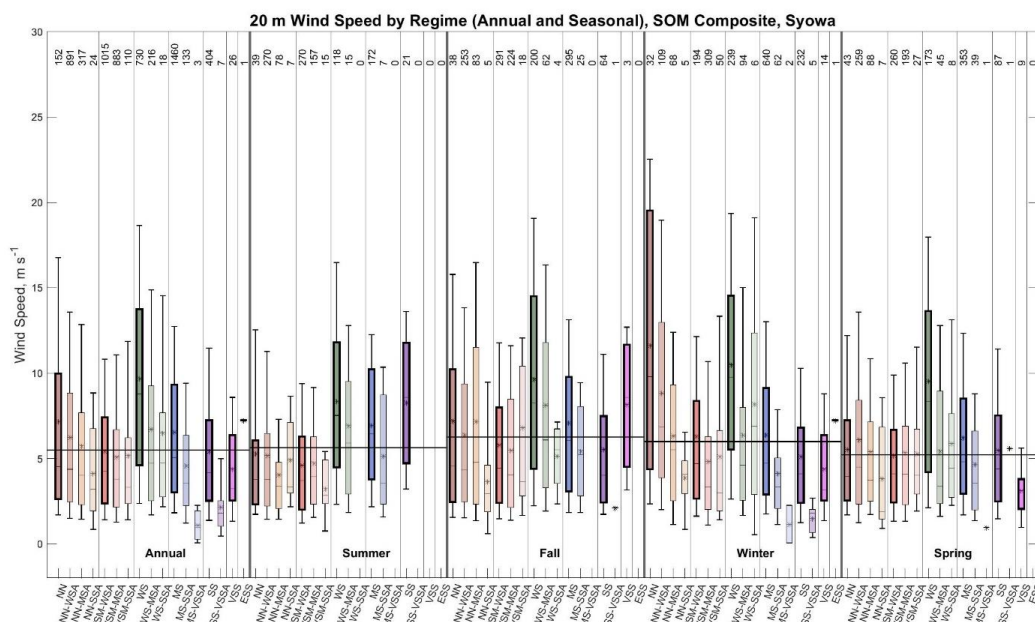
602 *Figure 11: Box plot showing the distribution of downwelling longwave radiation observed for each stability regime*
 603 *at Syowa annually (left panel) and seasonally (right four panels – summer, fall, winter, and spring). Box plots show*
 604 *median downwelling longwave radiation (horizontal line), 25th and 75th percentiles (edges of boxes), mean*
 605 *downwelling longwave radiation (center black star), 10th and 90th percentiles (outer black stars), and minimum*
 606 *and maximum (whiskers). The thin vertical black lines in the figure separate the stability groupings in each panel*
 607 *(annual or seasonal). The thin horizontal black lines across each panel (annual or seasonal), indicate the mean*
 608 *value for that entire time period. The numbers at the top indicate the number of radiosonde profiles in each regime.*

609 At Syowa, the 20 m wind speed is shown for each regime on an annual and seasonal basis in
 610 Figure 12 and Table S5. The clearest result from Figure 12 regarding the basic near-surface stability
 611 regimes is the relatively strong wind speeds in the WS regime in comparison to the other regimes,
 612 especially the NN and VSM-WSA regimes, annually and seasonally, except in winter when NN and WS



613 have similar strong winds. Annually, wind speeds are strongest in the WS basic near-surface stability
614 regime (9.7 m s^{-1}), weaker and similar between NN (7.2 m s^{-1}) and MS (6.5 m s^{-1}) regimes, and then
615 weakest and similar between the VSM-WSA, SS, and VSS (4.4 m s^{-1} to 5.4 m s^{-1}) regimes. A similar
616 pattern is observed in the fall. However, in the winter NN has slightly stronger winds than WS, and in
617 summer and spring, wind speeds in the NN and VSM-WSA regimes are similar. Like what was noted at
618 all the sites above as well, winds in the VSM-WSA regime are 31% to 43% weaker than those in the NN
619 and WS regimes on an annual basis and in the fall and winter. Wind speed in the VSM-WSA regime is
620 more like that in the NN regime in the summer and spring, but still over 45% weaker than those in the
621 WS regime. When considering WS and stronger stability regimes the wind speed generally decreases with
622 increasing stability. This can be seen in the fall and spring where wind speeds decrease, from WS (9.5 m
623 s^{-1} to 9.7 m s^{-1}) to SS (5.5 m s^{-1}), and from WS (10.5 m s^{-1}) to VSS (4.4 m s^{-1}) in the winter. However, in
624 the summer, while wind speeds decrease from WS (8.3 m s^{-1}) to MS (6.9 m s^{-1}), winds then increase to SS
625 (8.3 m s^{-1}).

626 As stability aloft increases in each stability grouping, wind speed decreases with increasing
627 stability on an annual basis and usually in the winter (Figure 12; Table S5). Wind speed also decreases
628 with increasing stability aloft in the WS and MS stability groupings in the fall and spring, and in the WS
629 group in the summer. This tendency for wind speed to decrease with increasing stability aloft is generally
630 opposite what was observed at the other sites discussed previously (Figures 4, 6, 8, and 10). This decrease
631 in wind speed with increasing stability aloft is usually less than 3 m s^{-1} , except in the winter in the NN
632 stability group (5.3 m s^{-1}) and in the winter and spring in the WS stability group (both decrease 4.1 m s^{-1}).
633 In the summer, fall, and spring as stability aloft increases wind speeds do not differ much in the NN and
634 VSM stability groupings. For example, wind speeds across the NN and VSM regimes in summer differ
635 only by 1.3 m s^{-1} to 1.4 m s^{-1} , and in fall, wind speed in the NN regime differ by less than 1 m s^{-1} .



636 *Figure 12: Box plot showing the distribution of 20 m wind speed observed for each stability regime at Syowa*
 637 *annually (left panel) and seasonally (right four panels – summer, fall, winter, and spring). Box plots show median*
 638 *20 m wind speed (horizontal line), mean 20 m wind speed (center black star), 25th and 75th percentiles (edges of*
 639 *boxes), and 10th and 90th percentiles (whiskers). The thin vertical black lines in the figure separate the stability*
 640 *groupings in each panel (annual or seasonal). The thin horizontal black lines across each panel (annual or*
 641 *seasonal), indicate the mean value for that entire time period. The numbers at the top indicate the number of*
 642 *radiosonde profiles in each regime.*

643 4 Discussion and Conclusions

644 To compare and synthesize the forcing mechanisms for varying boundary layer stability across
 645 the Antarctic continent from the individual sites presented in the previous section, Figure 13 shows the
 646 mean downwelling longwave radiation (left column) and 20 m wind speed (right column) for each
 647 stability grouping annually (panels a and b) and seasonally (panels c to j). Here, stability groupings are all
 648 stability regimes with the same near surface stability classification regardless of the aloft stability. For
 649 example, the mean forcing for the NN stability grouping would include all the NN regimes, regardless of
 650 aloft stability. To further simplify the results shown in this summary figure, any stability grouping which
 651 exhibits less than 10 observations total in each season has been omitted from this figure. For example,
 652 there is only one ESS observation at Neumayer and Syowa, both in the winter, so these stability
 653 groupings are not shown since the mean is likely not very representative.

654 Figure 13 (left column) shows downwelling longwave radiation generally decreases annually and
 655 seasonally with increasing stability from the NN to ESS stability groups, consistent with the results
 656 shown in Section 3 for all five study sites. Downwelling longwave radiation usually decreases from NN
 657 to VSM, and then slightly increases from VSM to WS. From WS to the strongest stability regime present
 658 at a given site in each season, downwelling longwave radiation then usually decreases, except in the
 659 summer at the continental interior sites where downwelling longwave radiation is similar across these
 660 regimes. It is hypothesized that in the summer, the diurnal cycle associated with solar radiation is

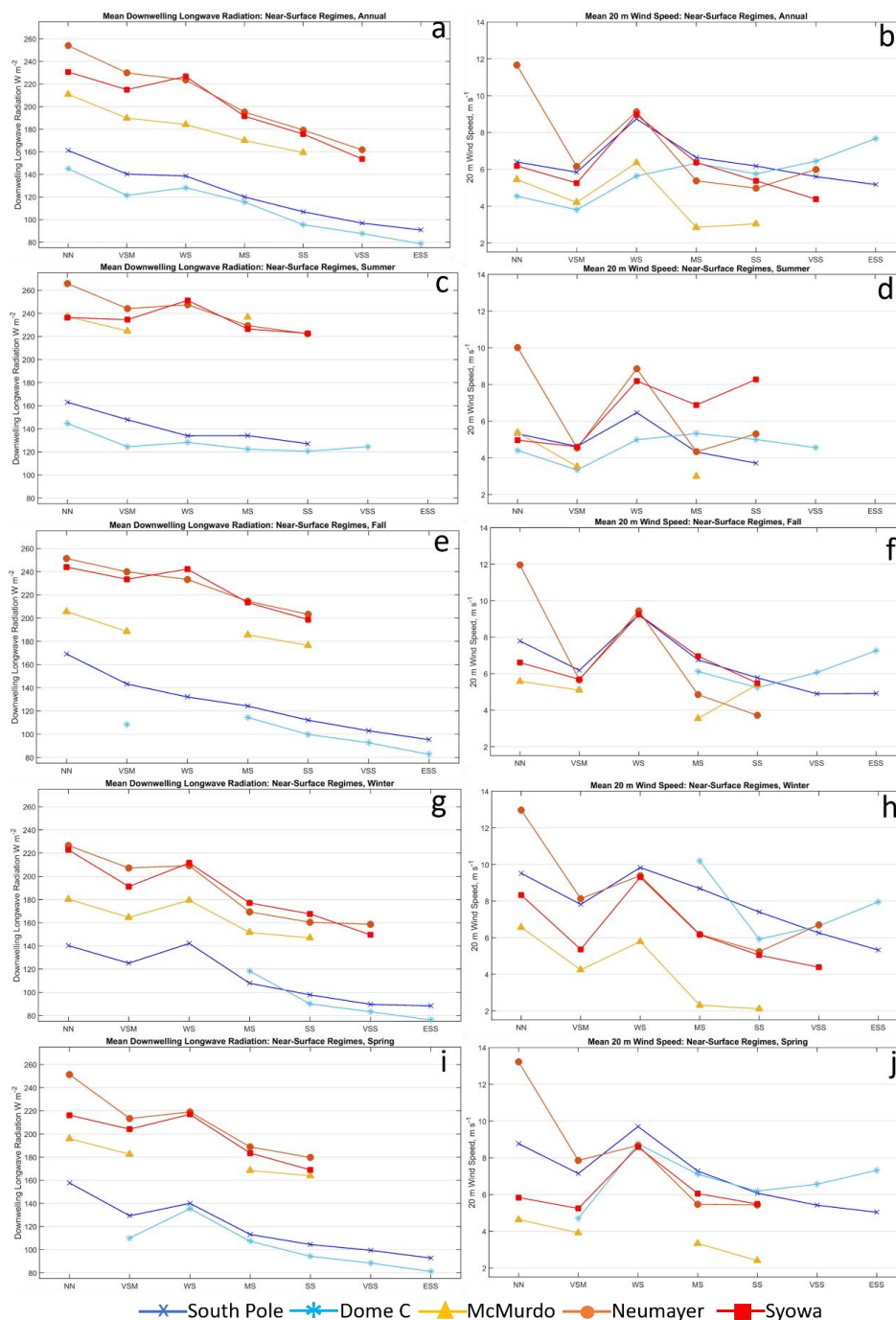


661 dominant, rather than downwelling longwave radiation, in driving changes in stability during this season,
662 unlike in the winter and transition seasons when changes in downwelling longwave radiation are more
663 able to quickly alter near-surface stability (Zhang et al., 2011). This was also observed by Pietroni et al.
664 (2013) who noted that the main forcing mechanism for stability in the summer at Dome C is likely the
665 influence of solar radiation during the summer months.

666 For the 20 m wind speed (Figure 13, right column), considering the first three stability regimes
667 (NN, VSM, and WS), wind speeds are usually strongest in the WS regime, except at Neumayer, while
668 wind speeds are more moderate in NN, and weakest in VSM. This is seen annually and seasonally and
669 highlights an important difference in forcing for the VSM regime in comparison to the NN and WS
670 regimes, from which VSM is derived, having the same potential temperature gradient as these regimes,
671 but with a much shallower boundary layer (Table 2). The relatively weaker winds in VSM in comparison
672 to NN and WS, which was also observed at all sites in Section 3, suggests there is less mechanical
673 generation of turbulence in this regime which results in a shallower boundary layer. At all sites except
674 Dome C, from WS to the strongest stability regime present in each season at a given site, the 20 m wind
675 speed usually decreases. The few exceptions to this behavior are at Neumayer, from SS to VSS annually
676 and in the winter, and from MS to SS in the summer. The increase in 20 m wind speed as stability
677 increases at Dome C is an unexpected result, as previous studies have shown that lower wind speeds are
678 usually associated with stronger stability (Hudson and Brandt, 2005; Cassano et al., 2016; Dice and
679 Cassano, 2022). A discussion as to why this behavior is observed will be given below.

680 Considering the combined effects of radiative forcing and mechanical mixing on boundary layer
681 stability for the NN, VSM and WS regimes we note unique forcing for each stability grouping. For the
682 NN regime, larger downwelling longwave radiation than in the VSM and WS groups results in reduced
683 surface cooling or possibly radiative heating, resulting in reduced near-surface stability. Also, the winds
684 in NN, which are usually more moderate in comparison to those in WS, also favor the near-neutral
685 stability of this regime (Cassano et al., 2016; Nigro et al., 2017). The WS regime usually has less
686 downwelling longwave radiation in comparison to the NN regime, which favors slightly enhanced
687 stability in comparison. The stronger winds in the WS regime, compared to NN and VSM, prevent
688 stability from being any stronger in the WS regime. The VSM regime has distinct radiative and
689 mechanical forcing compared to the NN and WS regimes. The VSM regime has mean downwelling
690 longwave radiation between that in the NN and WS regimes favoring stability that is intermediate to these
691 two regimes. The weaker winds in VSM compared to NN and WS result in less mechanical generation of
692 turbulence and a shallower boundary layer, which distinguishes this regime from the NN and WS
693 regimes.

694 In comparison, for the WS and stronger stability regimes it appears that the decrease in
695 downwelling longwave radiation, with increasing stability, is the primary forcing that leads to greater near
696 surface stability. For all sites, except Dome C, wind speed generally decreases with increasing stability
697 which also favors stronger near surface stability due to reduced mechanical mixing. The anomalous
698 results at Dome C will be discussed further below.



699 *Figure 13: Summary of the mean downwelling longwave radiation (left column) and 20 m wind speed*
 700 *(right column) for the near-surface stability regimes at all five sites annually (a and b) and seasonally:*
 701 *summer, fall, winter, and spring (c through j).*

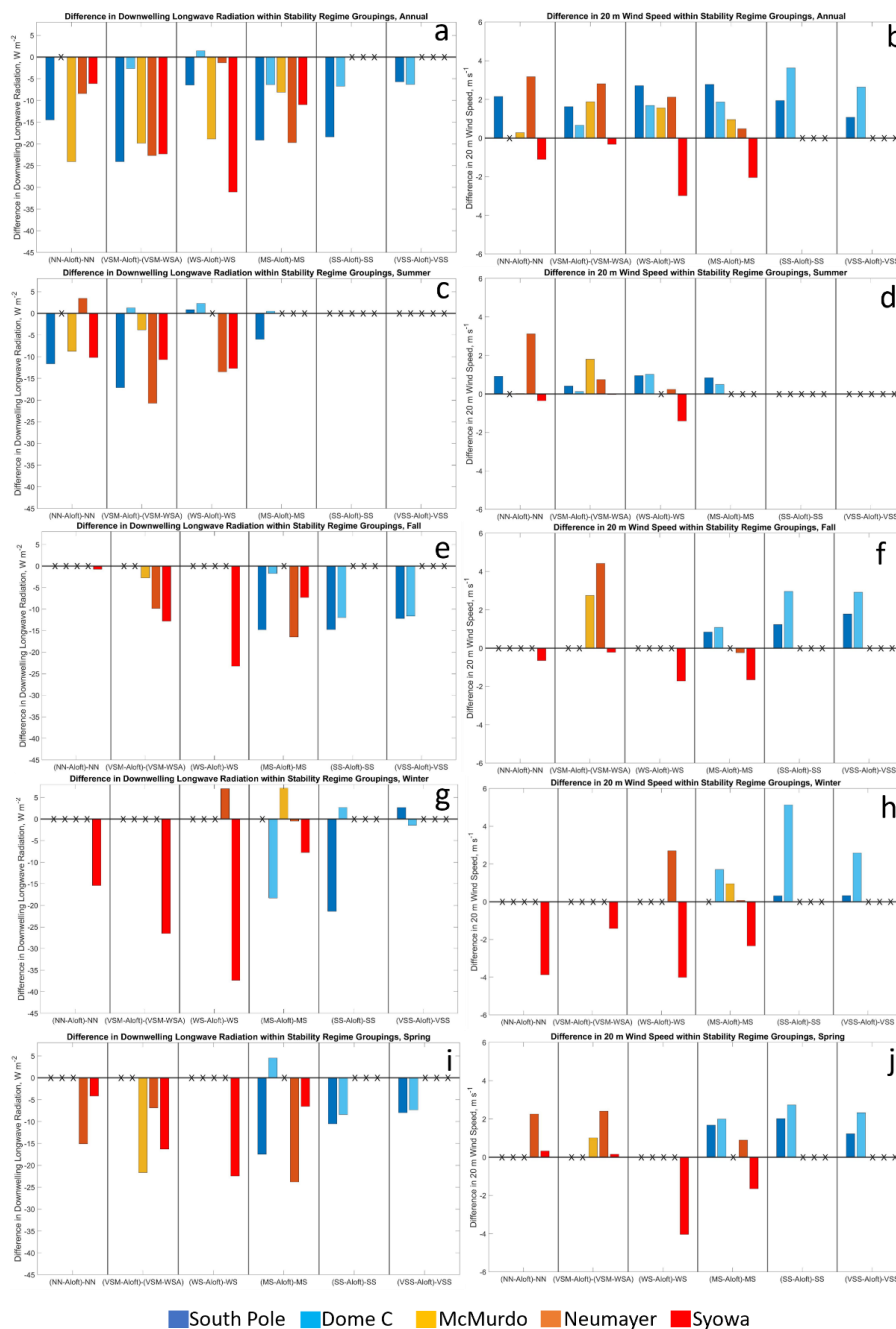


702 Next, we compare the forcing mechanisms for the basic near-surface stability regimes, with no
703 enhanced stability aloft, and regimes with the same near surface stability but enhanced stability aloft.
704 Figure 14 shows the differences in mean downwelling longwave radiation (left column) and 20 m wind
705 speed (right column) between each basic near-surface stability regime and those regimes with the same
706 near-surface stability but enhanced stability aloft. The difference is calculated as the mean downwelling
707 longwave radiation across, for example, NN-WSA, NN-MSA, and NN-SSA minus the mean
708 downwelling longwave radiation in NN. The magnitude (either positive or negative) of the bar indicates
709 this difference annually (a and b) and seasonally (c through j) for each site. As with Figure 13, any basic
710 near-surface stability regime or aloft groupings with less than 10 observations in has been omitted from
711 this figure and marked with an X.

712 The left column in Figure 14 shows that downwelling longwave radiation is almost always lower
713 for regimes with enhanced stability aloft compared to their basic near-surface stability regime
714 counterparts, indicated by the consistently negative bars annually and seasonally. These differences
715 mostly range from a few to 15 or more $W m^{-2}$. The magnitude of this negative difference when enhanced
716 stability is present aloft is usually larger at South Pole compared to Dome C, which usually has the
717 smallest (or about the same) difference compared to the other sites. Large differences also occur at
718 Neumayer in the summer for the VSM stability grouping (difference of about $22 W m^{-2}$), and the spring in
719 the MS stability grouping (difference of about $25 W m^{-2}$). The largest differences generally occur at
720 Syowa, especially in the winter where this difference reaches nearly $40 W m^{-2}$ in the WS stability
721 grouping.

722 The right column in Figure 14 shows that 20 m wind speed is almost always higher for regimes
723 with enhanced stability aloft compared to the basic near-surface stability regimes, except at Syowa, with
724 differences typically ranging from less than $0.5 m s^{-1}$ to about $2 m s^{-1}$. The magnitude of this difference is
725 usually larger at Dome C (usually between $1 m s^{-1}$ and $5 m s^{-1}$) compared to at South Pole (usually less
726 than $2 m s^{-1}$), especially when stability is MS and greater. In the summer, wind speed does not differ as
727 much between the basic and aloft regimes compared to the difference in the other seasons. In the summer,
728 the smaller difference in wind speed between the basic and aloft stability regimes in comparison to in the
729 other seasons, suggest that changes in wind speed are not as important in forcing changes in stability, but
730 rather, like what was noted above, changes in shortwave radiation contribute more to changes in near-
731 surface stability (Zhang et al., 2011; Pietroni et al., 2013). Unlike at the other sites, at Syowa (red bars)
732 wind speeds are always less when enhanced stability aloft is present, and the magnitude of this decrease is
733 usually as large or larger ($1 m s^{-1}$ to $4 m s^{-1}$) than the increases in wind speed seen at the other sites.

734 Considering both the radiative and mechanical forcing differences when enhanced stability aloft
735 is present provides insights into the mechanisms that results in stability regimes with stronger stability
736 above the surface. The reduced downwelling longwave radiation when there is enhanced stability aloft
737 (Figure 14) would suggest that near-surface stability should be stronger, like what was seen in Figure 13,
738 but instead stability near the surface remains the same with enhanced stability aloft. It is hypothesized that
739 the stronger near surface stability suggested by the reduced downwelling longwave radiation is unable to
740 form due to the stronger wind and associated mechanical mixing resulting in a layered stability profile,
741 with weaker stability near the surface and enhanced stability aloft. This suggested behavior is consistent
742 with previous research that found that as wind speed increases near surface stability is reduced (Hudson
743 and Brandt 2005; Pietroni et al., 2013; Cassano et al., 2016; Silva et al., 2022). The exception is the
744 anomalous behavior at Syowa, where wind speed is lower for regimes with enhanced stability aloft in
745 comparison to the basic near-surface stability regimes, and this will be discussed in more detail below.



746 *Figure 14: Summary of the difference in downwelling longwave radiation between the near-surface*
 747 *stability regimes and the mean of the aloft regimes (left column) and the same for 20 m wind speed (right*
 748 *column) at all five sites annually (a and b) and seasonally: summer, fall, winter and spring (c through j).*
 749 *An 'X' in place of a bar indicates fewer than 10 observations are present for either the basic or aloft*
 750 *variations in this regime and has not been included.*



751 The results discussed above confirm many of the expectations outlined in the introduction, that
752 downwelling longwave radiation decreases with increasing stability as does 20 m wind speed for regimes
753 WS and stronger (Figure 13). The specific forcing for the VSM regime was discovered to be slightly less
754 downwelling longwave radiation and weaker winds in comparison to the NN and WS regimes which
755 result in similar stability but less vertical mixing, and a shallower boundary layer. Figure 14 showed that
756 enhanced near-surface winds counteract the reduced downwelling longwave radiation when enhanced
757 stability aloft is present, allowing weaker near-surface stability to persist while enhanced stability is
758 present aloft. There were also some unexpected results, namely the increase in wind speed with increasing
759 stability at Dome C (Figure 13, right column), and the lower wind speeds with enhanced stability aloft
760 compared to the basic near-surface stability regimes at Syowa (Figure 14, right column). These
761 anomalous findings will now be further discussed.

762 At Dome C, a strong decrease in downwelling longwave radiation with increasing stability in the
763 winter, fall, and spring is likely responsible for driving changes in stability during these seasons (Figure 5
764 and Figure 13), while changes in shortwave radiation likely control stability changes during the summer
765 (Zhang et al., 2011; Pietroni et al., 2013). Stone and Kahl (1991) found surface warming and reduced
766 stability with enhanced downwelling longwave radiation, and that variations in downwelling longwave
767 radiation are responsible for most of the variations in changing surface conditions and stability at the
768 South Pole. This is also consistent with the observations here from the continental interior, particularly at
769 Dome C. Additionally, Pietroni et al. (2013) found changes in stability in the winter at Dome C to be
770 mostly attributed to sudden increases downwelling longwave radiation. The unexpected result at Dome C
771 is that wind speed increases with increasing stability, counter to previous results (Hudson and Brandt
772 2005; Pietroni et al., 2013; Cassano et al., 2016; Silva et al., 2022).

773 It is hypothesized that the stronger wind speed with increasing stability is not contributing to the
774 formation of the stability regimes, but rather that the increase in wind speed is a response to the greater
775 stability. The very low values of downwelling longwave radiation at Dome C led to strong surface
776 cooling and the development of strong stability, especially immediately adjacent to the ice surface, which
777 resulted in weak or intermittent turbulence (Pietroni et al., 2013; Zhang et al., 2011). With little
778 turbulence, frictional slowing of the wind will be reduced, and 20 m winds could increase with increasing
779 stability. The reason this behavior occurs at Dome C, but is not observed at the other sites, is unclear. It
780 may be due to the very strong radiative cooling at this highest elevation site considered in this study.
781 Also, unlike the other sites, Dome C is almost flat so no katabatic flow can develop to advect away the
782 radiatively cooled air adjacent to the surface, allowing strong stability to grow with time while turbulence
783 is suppressed.

784 At Syowa, unlike at the other sites, wind speed was less when enhanced stability aloft was present
785 and does not follow the conclusion that increased wind speed is responsible for reducing near surface
786 stability (Figure 14). This leaves to question the forcing mechanism for regimes with enhanced stability
787 above a layer of weaker near-surface stability at Syowa. We suggest that the answer is likely related to the
788 complex katabatic and cyclonic influences that are present at Syowa and have been shown to impact the
789 boundary layer conditions at this site (Murakoshi, 1958; Tomikawa et al., 2015; Yamada and Hirasawa,
790 2018). At Syowa, easterly winds are associated with windy, cyclonic activity and weak near-surface
791 stability, while southerly or southwesterly winds are associated with calm, non-cyclonic conditions and
792 moderate to strong stability (Tomikawa et al., 2015; Yamada and Hirasawa, 2018). Supplemental Figure 1
793 provides some insight for this by showing the range of wind direction observed for each stability regime
794 annually and seasonally at Syowa. As stability aloft increases in each stability grouping, the wind
795 direction changes from easterly to more southeasterly. As the wind direction shifts from easterly to



796 southeasterly the wind has a more continental origin and is likely colder. This suggests that weak drainage
797 flow from the continental interior may be advecting cold air at low levels, while more mild, maritime air
798 remains aloft, resulting in profiles with enhanced stability aloft at the interface between the cold
799 continental air at low levels and the mild maritime air above.

800 Here, the forcing mechanisms for the variations in boundary layer stability described by Dice et
801 al. (2023) were identified for two continental interior sites and three coastal sites in Antarctica. Boundary
802 layer stability and the forcing mechanisms that drive variations in boundary layer stability is widely
803 misrepresented in weather and climate models (e.g., Genthon et al., 2013; Holtslag et al., 2013; Mahrt,
804 2014). A next step in this work will be to assess the ability of the Antarctic Mesoscale Prediction System
805 (AMPS) (Powers et al., 2012) to simulate the frequency of boundary layer stability regimes (Dice et al.,
806 2023) and differing forcing for each stability regime.

807 **Data Availability**

808 The data used to support this project can be found at:

809 McMurdo:

810 All data: https://adc.arm.gov/discovery/#/results/site_code::awr.

811 Syowa:

812 Radiosonde data: Office of Antarctic Observation Japan Meteorological Agency (pers. comm.
813 Yutaka Ogawa)

814 Radiation data: <https://doi.pangaea.de/10.1594/PANGAEA.956748>

815 Dome C:

816 Radiosonde data: <https://www.climantartide.it/dataaccess/index.php?lang=it>

817 Radiation data: <https://doi.pangaea.de/10.1594/PANGAEA.935421>

818 South Pole:

819 Radiosonde data: <http://amrc.ssec.wisc.edu/data/ftp/pub/southpole/radiosonde/>

820 Radiation data: <https://doi.pangaea.de/10.1594/PANGAEA.956847>

821 Neumayer:

822 Radiosonde data: <https://doi.org/10.1594/PANGAEA.940584>

823 Radiation data: <https://doi.org/10.1594/PANGAEA.940584>

824 **Competing Interests**

825 The contact author has declared that none of the authors has any competing interests.

826 **Acknowledgements**

827 Funding for this work came from the United States National Science Foundation (NSF) grant OPP
828 1745097 and the National Aeronautics and Space Administration (NASA; award 80NSSC19M0194). The
829 authors thank the United States Antarctic Program, the Department of Energy, the Baseline Surface
830 Radiation Network, the Antarctic Meteorological Research and Data Center, the Antarctic Meteo-



831 Climatological Observatory, and the Office of Antarctic Observation Japan Meteorological Agency for
832 the support and logistics for the data used in this paper.

833 **References**

834 Andreas, E.L., Claffy, K.J., and Makshtas, A.P.: Low-level atmospheric jets and inversions over the
835 western Weddell Sea, *Boundary-Layer Meteorology*, 97, 459-486, doi:10.1023/A:1002793831076, 2000.

836 ARGENTINI, S., VIOLA, A., SEMPREVIVA, A. M., & PETENKO, I.: Summer boundary-layer height
837 at the plateau site of Dome C, Antarctica. *Boundary - Layer Meteorology*, 115(3), 409–422, DOI
838 10.1007/s10546-004-5643-6, 2005.

839 Cassano, E.N., Glisan, J.M., Cassano, J.J., Gutowski, W.J. Jr., and Seefeldt, M.W.: Self-organizing map
840 analysis of widespread temperature extremes in Alaska and Canada, *Climate Research*, 62, 199-218,
841 <https://doi.org/10.3354/cr01274>, 2015.

842 Cassano, J. J., Nigro, M., and Lazzara, M.: Characteristics of the near surface atmosphere over the Ross
843 ice shelf, Antarctica, *Journal of Geophysical Research: Atmospheres*, 121, 3339-3362,
844 <https://doi.org/10.1002/2015JD024383>, 2016.

845 Dice, M. J., and Cassano, J. J.: Assessing physical relationships between atmospheric state, fluxes, and
846 boundary layer stability at McMurdo Station, Antarctica, *Journal of Geophysical Research: Atmospheres*,
847 127, e2021JD036075. <https://doi.org/10.1029/2021JD036075>, 2022.

848 Dice, M. J. and Cassano, J. and Jozef, G. C. and Seefeldt, M.: Variations in Boundary Layer Stability
849 Across Antarctica: A Comparison Between Coastal and Interior Sites, *EGU Sphere*, 2023, 1-35,
850 10.5194/egusphere-2023-1673, 2023.

851 Ganeshan, M., Yang, Y., and Palm, S. P.: Impact of clouds and blowing snow on surface and atmospheric
852 boundary layer properties over Dome C, Antarctica. *Journal of Geophysical Research: Atmospheres*, 127,
853 e2022JD036801. <https://doi.org/10.1029/2022JD036801>, 2022.

854 Genthon, C., Six, D., Gallée, H., Grigioni, P., and Pellegrini, A.: Two years of atmospheric boundary
855 layer observations on a 45-m tower at Dome C on the Antarctic plateau, *Journal of Geophysical Research:*
856 *Atmospheres*, 118, 3218-3232, doi:10.1002/jgrd.50128, 2013.

857 Holtstag, A. A. M., Svensson, G., Baas, P., Basu, S., Beare, B., Beljaars, A. C. M., Bosveld, F. C.,
858 Cuxart, J., Lindvall, J., Steeneveld, G. J., Tjernström, M., and Van De Wiel, B. J. H.: STABLE
859 ATMOSPHERIC BOUNDARY LAYERS AND DIURNAL CYCLES: Challenges for Weather and
860 Climate Models. *Bulletin of the American Meteorological Society*, 94(11), 1691–1706, 2013

861 Hudson, S., and Brandt, R.: A look at the surface-based temperature inversion on the Antarctic Plateau,
862 *Journal of Climate*, 18, 1673-1696, <https://doi.org/10.1175/JCLI3360.1>, 2005.

863 Jozef, G., Cassano, J., Dahlke, S., and de Boer, G.: Testing the efficacy of atmospheric boundary layer
864 height detection algorithms using uncrewed aircraft system data from MOSAiC, *Atmospheric*
865 *Measurement Techniques*, 15, 4001-4022, <https://doi.org/10.5194/amt-15-4001-2022>, 2022.

866 Jozef, G. C., Cassano, J. J., Dahlke, S., Dice, M., Cox, C. J., and de Boer, G.: An Overview of the
867 Vertical Structure of the Atmospheric Boundary Layer in the Central Arctic during MOSAiC, *EGUsphere*
868 [preprint], <https://doi.org/10.5194/egusphere-2023-780>, 2023.



- 869 King, J. C. and Turner, J.: Antarctic Meteorology and Climatology, Cambridge Atmospheric and Space
870 Sciences Series, Cambridge University Press, U.K., 1997.
- 871 Lazzara, M. A., L. M. Keller, T. Markle, and J. Gallagher.: Fifty-year Amundsen-Scott South Pole station
872 surface climatology. *Atmos. Res.*, 118, 240–259, <https://doi.org/10.1016/j.atmosres.2012.06.027>, 2012.
- 873 Lubin, D., Bromwich, D. H., Vogelmann, A. M., Verlinde, J., and Russell, L. M.: ARM West Antarctic
874 Radiation Experiment (AWARE) Field Campaign Report, DOE/SC-ARM-17-028, 2017.
- 875 Lubin, D., Zhang, D., Silber, I., Scott, R. C., Kalogeras, P., Battaglia, A., et al.: AWARE: The
876 atmospheric radiation measurement (ARM) West Antarctic radiation experiment. *Bulletin of the*
877 *American Meteorological Society*, 101, E1069-E1091, <https://doi.org/10.1175/BAMS-D-18-0278.1s>,
878 2020.
- 879 Mahesh, A., Walden, V. P., and Warren, S. G.: Radiosonde Temperature Measurements in Strong
880 Inversions: Correction for Thermal Lag Based on an Experiment at the South Pole, *Journal of*
881 *Atmospheric and Oceanic Technology*, 14, 45-53. [https://doi.org/10.1175/1520-
882 0426\(1997\)014<0045:RTMISI>2.0.CO;2](https://doi.org/10.1175/1520-0426(1997)014<0045:RTMISI>2.0.CO;2), 1997.
- 883 Mahrt, L.: Stably Stratified Atmospheric Boundary Layers, *Annual review of fluid mechanics*, 46, 23-45,
884 doi:10.1146/annurev-fluid-010313-141354, 2014.
- 885 Matsuoka, K., Skoglund, A., and Roth, G.: Quantarctica [data set]. Norwegian Polar Institute.
886 <https://doi.org/10.21334/npolar.2018.8516e961>, 2018.
- 887 Murakoshi, N.: Meteorological observations at the Syowa base during the period from March 1957 to
888 February 1958, Japan Meteorological Agency, doi/10.15094/00006856, 1958.
- 889 Nigro, M. A., Cassano, J. J., Wille, J., Bromwich, D. H., and Lazzara, M. A.: A Self-Organizing-Map-
890 Based Evaluation of the Antarctic Mesoscale Prediction System Using Observations from a 30-m
891 Instrumented Tower on the Ross Ice Shelf, *Antarctica, Weather and Forecasting*, 32, 223-242,
892 <https://doi.org/10.1175/WAF-D-16-0084.1>, 2017.
- 893 Phillpot, H. R., and Zillman, J. W.: The surface temperature inversion over the Antarctic
894 continent, *Journal of Geophysical Research*, 75, 4161-4169, <https://doi.org/10.1029/JC075i021p04161>,
895 1970.
- 896 Pietroni, I., Argentini, S., and Petenko, I.: One Year of Surface-Based Temperature Inversions at Dome C,
897 Antarctica. *Boundary Layer Meteorology*, 150, 131-151, DOI 10.1007/s10546-013-9861-7, 2013.
- 898 Powers, J. G., Manning, K. W., Bromwich, D. H., Cassano, J. J., and Cayette, A. M.: A Decade of
899 Antarctic Science Support Through AMPS, *Bulletin of the American Meteorological Society*, 93, 1699-
900 1712, doi: <https://doi.org/10.1175/BAMS-D-11-00186.1>, 2012.
- 901 Rodrigo, J. S., and, P. S.: Investigation of the stable atmospheric boundary layer at Halley
902 Antarctica. *Boundary-Layer Meteorology*, 148, 517–539. <https://doi.org/10.1007/s10546-013-9831-0>,
903 2013.
- 904 Schwartz, B. E., and Doswell, C. A., III.: North American Rawinsonde Observations: Problems,
905 Concerns, and a Call to Action, *Bulletin of the American Meteorological Society*, 72, 1885-1896,
906 [https://doi.org/10.1175/1520-0477\(1991\)072<1885:NAROPC>2.0.CO;2](https://doi.org/10.1175/1520-0477(1991)072<1885:NAROPC>2.0.CO;2), 1991.



- 907 Seefeldt, M. W., and Cassano, J. J.: A description of the Ross Ice Shelf air stream (RAS) through the use
908 of self-organizing maps (SOMs), *J. Geophys. Res.*, 117, D09112, doi:10.1029/2011JD016857, 2012.
- 909 Silber, I., Verlinde, J., Eloranta, E. W., and Cadet, M.: Antarctic Cloud macrophysical, thermodynamic
910 phase, and atmospheric inversion coupling properties at McMurdo station: I. Principal data processing
911 and climatology. *Antarctic cloud macrophysical, thermodynamic phase, and atmospheric inversion*
912 *coupling properties at McMurdo Station: I, Principal data processing and climatology*, United States, 123,
913 6099-6121, <https://doi.org/10.1029/2018JD028279>, 2018.
- 914 Silva, T., Schlosser, E., and Lehner, M.: A 25-year climatology of low-tropospheric temperature and
915 humidity inversions for contrasting synoptic regimes at Neumayer Station, Antarctica, *International*
916 *Journal of Climatology*, 43, 456-479, <https://doi.org/10.1002/joc.7780>, 2022.
- 917 Solomon, A., Shupe, M.D., Svensson, G., Barton, N.P., Batrak, Y., Bazile, E., Day, J.J., Doyle, J.D.,
918 Frank, H.P., Keeley, S., Remes, T., Tolstykh, M.: The winter central Arctic surface energy budget: A
919 model evaluation using observations from the MOSAiC campaign. *Elementa: Science of the*
920 *Anthropocene*; 11, 00104, doi: <https://doi.org/10.1525/elementa.2022.00104>, 2023
- 921 Stone, R. S., and Kahl, J. D.: Variations in boundary layer properties associated with clouds and transient
922 weather disturbances at the South Pole during winter, *Journal of Geophysical Research*, 96, 5137-5144,
923 doi:10.1029/90JD02605, 1991.
- 924 Stull, R. B.: *An Introduction to Boundary Layer Meteorology*, Springer, 1988.
- 925 Tomikawa, Y., Nomoto, M., Miura, H., Tsutsumi, M., Nishimura, K., Nakamura, T., Yamagishi, H.,
926 Yamanouchi, T., Sato, T., and Sato, K.: Vertical Wind Disturbances during a Strong Wind Event
927 Observed by the PANSY Radar at Syowa Station, Antarctica. *Monthly Weather Review*, 143(5), 1804–
928 1821, DOI: 10.1175/MWR-D-14-00289.1, 2015.
- 929 Vignon, E., van de Wiel, B. J. H., van Hooijdonk, I. G. S., Genthon, C., van der Linden, S. J. A., van
930 Hooft, J. A., Baas, P., Maurel, W., Traulle, O., and Casasanta, G.: Stable boundary-layer regimes at Dome
931 C, Antarctica: observation and analysis, *Quarterly Journal of the Royal Meteorological Society*, 143,
932 1241, <https://doi.org/10.1002/qj.2998>, 2017.
- 933 Vihma, T., E. Tuovinen, and H. Savijärvi: Interaction of katabatic winds and near-surface temperatures in
934 the Antarctic, *J. Geophys. Res.*, 116, D21119, doi:10.1029/2010JD014917, 2011.
- 935 Yamada, K., and Hirasawa, N.: of a Record-Breaking Strong Wind Event at Syowa Station in January
936 2015, *Journal of Geophysical Research: Atmospheres*, 123, 13643-13657.
937 <https://doi.org/10.1029/2018JD028877>, 2018.
- 938 Zhang, Y., Seidel, D., Golaz, J., Deser, C., and Tomas, R.: Climatological characteristics of Arctic and
939 Antarctic surface-based inversions, *Journal of Climate*, 24, 5167-5186.
940 <https://doi.org/10.1175/2011JCLI4004.1>, 2011.